



Meteorological conditions in the central Arctic summer during the Arctic Summer Cloud Ocean Study (ASCOS)

M. Tjernström^{1,2}, C. E. Birch³, I. M. Brooks³, M. D. Shupe^{4,5}, P. O. G. Persson^{4,5}, J. Sedlar⁶, T. Mauritsen⁷, C. Leck^{1,2}, J. Paatero⁸, M. Szczodrak⁹, and C. R. Wheeler⁴

¹Department of Meteorology, Stockholm University, Stockholm, Sweden

²Bert Bolin Center for Climate Research, Stockholm University, Sweden

³Institute for Climate & Atmospheric Science, School of Earth and Environment, University of Leeds, Leeds, UK

⁴Cooperative Institute for Research in the Environmental Sciences (CIRES), University of Colorado, Boulder, CO, USA

⁵National Atmospheric and Oceanic Administration, Physical Sciences Division, Boulder, Colorado, USA

⁶Swedish Meteorological and Hydrological Institute, Norrköping, Sweden

⁷Max Planck Institute for Meteorology, Hamburg, Germany

⁸Finnish Meteorological Institute, Helsinki, Finland

⁹Rosenstiel School of Marine and Atmospheric Sciences, University of Miami, Miami, USA

Correspondence to: M. Tjernström (michaelt@misu.su.se)

Received: 19 December 2011 – Published in Atmos. Chem. Phys. Discuss.: 3 February 2012

Revised: 7 June 2012 – Accepted: 25 June 2012 – Published: 1 August 2012

Abstract. Understanding the rapidly changing climate in the Arctic is limited by a lack of understanding of underlying strong feedback mechanisms that are specific to the Arctic. Progress in this field can only be obtained by process-level observations; this is the motivation for intensive ice-breaker-based campaigns such as the Arctic Summer Cloud-Ocean Study (ASCOS), described here. However, detailed field observations also have to be put in the context of the larger-scale meteorology, and short field campaigns have to be analysed within the context of the underlying climate state and temporal anomalies from this.

To aid in the analysis of other parameters or processes observed during this campaign, this paper provides an overview of the synoptic-scale meteorology and its climatic anomaly during the ASCOS field deployment. It also provides a statistical analysis of key features during the campaign, such as key meteorological variables, the vertical structure of the lower troposphere and clouds, and energy fluxes at the surface. In order to assess the representativity of the ASCOS results, we also compare these features to similar observations obtained during three earlier summer experiments in the Arctic Ocean: the AOE-96, SHEBA and AOE-2001 expeditions.

We find that these expeditions share many key features of the summertime lower troposphere. Taking ASCOS and

the previous expeditions together, a common picture emerges with a large amount of low-level cloud in a well-mixed shallow boundary layer, capped by a weak to moderately strong inversion where moisture, and sometimes also cloud top, penetrate into the lower parts of the inversion. Much of the boundary-layer mixing is due to cloud-top cooling and subsequent buoyant overturning of the cloud. The cloud layer may, or may not, be connected with surface processes depending on the depths of the cloud and surface-based boundary layers and on the relative strengths of surface-shear and cloud-generated turbulence. The latter also implies a connection between the cloud layer and the free troposphere through entrainment at cloud top.

1 Introduction

The rapidly changing Arctic climate (ACIA, 2005; IPCC, 2007; Richter-Menge and Jeffries, 2011) has focused scientific attention on this region. Arctic near-surface temperatures are rising at a rate more than twice that of the global average (e.g. Richter-Menge and Jeffries, 2011) and the perennial Arctic sea-ice is declining in all seasons, but most dramatically in summer (e.g. Lindsay and Zhang, 2005; Serreze

et al., 2007; Overland, 2009). Many aspects of the Arctic climate show an “Arctic amplification” (Serreze and Francis, 2006) and although no consensus exists about primary reasons for this, it is likely related to feedbacks in the Arctic climate system, some of which are related to clouds and surface albedo.

Climate modeling is an indispensable tool for understanding the complex climate system. However, state-of-the-art global climate models have significant problems with the Arctic (Walsh et al., 2002; Chapman and Walsh, 2007). For example, the inter-model spread in climate projections for the end of this century in the Intergovernmental Panel on Climate Change Fourth Assessment Report (IPCC-AR4) is largest in the Arctic (Holland and Bitz, 2003). Contributing to this is a combination of a large inherent variability and modeling uncertainties resulting from a poor understanding of important feedback mechanisms (e.g. Sorteberg et al., 2005). The effects of Arctic clouds lie at the heart of the Arctic amplification discussion (Liu et al., 2008; Kay et al., 2008; Kay and Gettelman, 2009).

Low-level clouds are ubiquitous in the Arctic, especially during the summer half of the year with monthly averaged cloud fraction as large as 80–90 % (Curry and Ebert, 1992; Wang and Key, 2005; Tjernström, 2005; Shupe et al., 2005, 2011). These clouds have a substantial effect on the surface energy budget (e.g. Intrieri et al., 2002a; Shupe and Intrieri, 2004; Sedlar et al., 2011) and thus on the melting and freezing of perennial sea ice (Kay and Gettelman, 2009). In contrast to similar clouds at lower latitudes, low-level clouds in the central Arctic tend to warm the surface relative to clear conditions most of the year (Intrieri et al., 2002b; Tjernström et al., 2004a). This is due to an intricate balance between the optical properties of the clouds and a highly reflecting surface (e.g. Sedlar et al., 2011).

Arctic clouds present a particular problem to modeling (Walsh et al., 2002; Tjernström et al., 2005, 2008; Karlsson and Svensson, 2010). Our lack of understanding of Arctic clouds and their effects limits the ability of climate models to simulate the current climate and therefore to provide future projections, and greatly hinders our understanding of the Arctic climate system. Simulating clouds directly in climate models is impossible; they must be parameterized as functions of variables resolved on a coarse model grid. Developing parameterizations requires an adequate understanding of the processes involved and ultimately relies on closure assumptions derived from process-level observations. New schemes also require testing against Arctic data. Such work is limited by the paucity in the central Arctic of process-level observations and hence obtaining in-situ observations in the Arctic and cloud-related processes over the central Arctic Ocean is crucial. While monitoring of climate in the remote central Arctic rests on remote sensing from satellites, again there is a lack of in-situ observations for developing and testing remote sensing techniques.

To contribute to the much-needed process-level in-situ data, several observational field programs have been conducted in the central Arctic Ocean but only one extensive experiment covers a full annual cycle: the Surface Heat Budget of the Arctic Ocean (SHEBA: Uttal et al., 2002), from fall 1997 to fall 1998. The Russian drifting “North Pole” stations (NP-stations, e.g. Kahl et al., 1996, 1999; Serreze et al., 1992) have made many basic meteorological observations in all parts of the year but obtained few process-level observations, especially related to cloud properties. The same limitation applies to the Tara expedition (Gascard et al., 2008), also covering a full annual cycle. Most other experiments have focused on the summer season, at least partly because the Arctic Ocean is reasonably accessible with icebreakers in summer.

The Arctic Summer Cloud Ocean Study (ASCOS) is the latest and most extensive in a series of summer expeditions with an atmospheric focus deployed on the Swedish icebreaker *Oden*. The previous experiments include the International Arctic Ocean Expedition 1991 (IAOE-91, Leck et al., 1996), the Arctic Ocean Expedition 1996 (AOE-96, Leck et al., 2001) and the Arctic Ocean Experiment 2001 (AOE-2001, Leck et al., 2004; Tjernström et al., 2004a, b). ASCOS was deployed in the summer of 2008, as a part of the 2007–2009 International Polar Year (IPY). ASCOS was the most extensive in-situ atmospheric Arctic Ocean experiment during the IPY, lasting over a month in the North Atlantic sector of the central Arctic Ocean. Activities were centered on a three-week ice-drift operation near 87° N, with the icebreaker moored to a drifting ice floe from mid-August through the beginning of September. Figure 1 shows the track of the expedition.

While short observation campaigns cannot be used to detect climate trends, the utility of shorter expeditions lies in the detailed studies of important processes that are possible with extensive short-term observations. Such data can be used to inform the development of better models and while simultaneously studying several detailed processes, it can also increase the understanding of the Arctic climate system. However, such short-term process studies must also be put into a larger context, precisely because they are short. The atmosphere is highly variable on many time scales and findings from process-level observations must be interpreted within the context of the prevailing larger-scale atmospheric circulation. It is also necessary to understand how representative observations from a short period are. Therefore, new observations must be cautiously placed within the context of already existing observations.

This paper presents a summary of the meteorological conditions encountered during ASCOS, from the synoptic scale down to boundary-layer scales, to aid in interpretation of more detailed process studies. We also compare ASCOS conditions with climatological means and anomalies and also contrast ASCOS observations to results from three of the earlier summer experiments discussed above. Detailed analyses

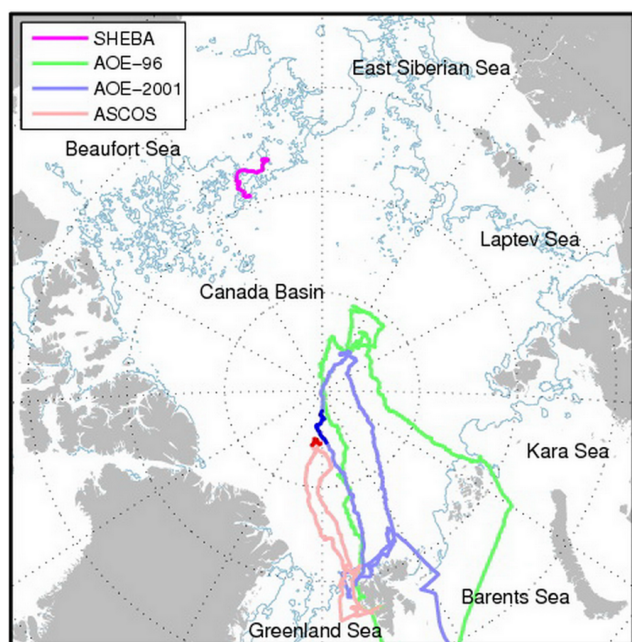


Fig. 1. Map with expedition tracks for ASCOS (red), the Arctic Ocean Experiment 2001 (AOE-2001; blue), the Arctic Ocean Experiment 1996 (AOE-96; green) and the Surface Heat Balance of the Arctic (SHEBA; magenta, July and August only). Ice-drift portions of the tracks are marked by darker color while the thin blue line is the approximate 12 August 2008 ice boundary.

of the larger-scale meteorology for these other experiments are published in overview papers from these expeditions (see Leck et al., 2001; Uttal et al., 2002; Tjernström et al., 2004a). A detailed analysis of reasons for differences or similarities between ASCOS and these earlier expeditions is, however, beyond the scope of this paper.

This paper is organized with a brief description of ASCOS and the data used in this study in Sect. 2 and a discussion of the large-scale atmospheric setting and transport characteristics during ASCOS in Sect. 3. Section 4 presents some basic meteorological characteristics from ASCOS, comparing these to results from the other experiments, while Sect. 5 describes some of the main characteristics of the ASCOS ice drift. A summary and conclusions is found in Sect. 6.

2 Data

2.1 The ASCOS experiment

The over-arching objective of ASCOS is to understand the formation and life cycle of low-level clouds and the role these play in the surface energy budget of the central Arctic Ocean, especially during the transition from late summer to early fall. Like its predecessors (IAOE-91, AOE-96 and AOE-2001), ASCOS was conducted onboard the Swedish icebreaker *Oden*. The expedition departed Longyearbyen on

Svalbard on 2 August (DoY¹ 214), returning on 9 September (DoY 253), 2008. By 12 August (DoY 225), after a few brief research stations in open water and the marginal ice zone and a transit north into the pack ice, *Oden* was moored to a 3 × 6 km large ice floe with which it drifted for 21 days. The ASCOS track is shown in Fig. 1; the drift track was from approximately 87°21' N 01°29' W to 87°09' N 11°01' W.

Operational meteorological analysis and forecasts for the expedition were supplied by the European Centre for Medium Range Weather Forecasts (ECMWF) for large-scale forecasts and the UK Met Office for detailed column forecasts. In this paper we use the ECMWF analyses while the UK Met Office Unified Model forecasts are presented and analyzed in Birch et al. (2012). To compare ASCOS conditions to climatology we use the NCAR/NCEP reanalysis products available from the National Oceanographic and Atmospheric Administration/Earth System Research Laboratory (NOAA/ESRL; <http://www.esrl.noaa.gov/psd>). Back-trajectories at six-hourly temporal resolution were calculated after the expedition using HYSPLIT (<http://ready.arl.noaa.gov/HYSPLIT.php>), and are based on analyzed meteorological fields from the National Center for Environmental Prediction's Global Data Assimilation System (NCEP/GDAS).

Table 1 summarizes the different sources of data from all four expeditions used in this study. For ASCOS, basic meteorology parameters were extracted from *Oden's* weather station (Tjernström, 2004b) complemented by a WeatherPak station installed onboard and from the micro-meteorology deployment on the ice during the ice drift; see Sedlar et al. (2011) for a description of the micrometeorology observations. Analyses of tropospheric vertical structure, clouds and frontal zones rest on the 6-hourly radiosoundings and on the MilliMeter wave-length Cloud Radar (MMCR, Moran et al., 1998) installed on the *Oden*. Additional information on the clouds came from several laser ceilometers, while additional temperature profile information came from a 60GHz scanning microwave radiometer (Westwater et al., 1999). Visibility was provided by a backscatter visibility sensor that was part of the *Oden* weather station (Tjernström et al., 2004b). Observations of surface radiation fluxes came from broadband pyranometers and pyrgeometers deployed on the ice, complemented by similar instruments on the *Oden*; net surface radiation was only measured on the ice. Turbulent heat fluxes were derived from eddy-correlation measurements made on two micrometeorology masts on the ice. Many other instrument systems were deployed during ASCOS but are not used here.

¹Throughout ASCOS, time is usually given as decimal day-of-the-year (DoY), defined so that DoY = 1.0 occurs at 00:00 UTC on 1 January.

Table 1. Brief overview of measurements used for the comparison between the different expeditions.

| Variables | Expedition | | | |
|---|---|---|--|--|
| | ASCOS | AOE-2001 | SHEBA | AOE-96 |
| Near-surface temperature, humidity and wind speed | Weather station onboard and mast on the ice | Weather station onboard and mast on the ice | Mast on the ice | Weather station onboard |
| Vertical thermodynamic structure | Radiosoundings (145) ^a | Radiosoundings (118) ^a | Radiosoundings (125) ^a | Radiosoundings (44) ^a |
| Inversion statistics | Scanning microwave radiometer | Scanning microwave radiometer | Radiosoundings | N/A ^b |
| Clouds | Laser ceilometer and MMCR | Laser ceilometer and Sband radar | MMCR and DABUL lidar | Laser ceilometer |
| Precipitable water & cloud liquid and ice water paths | Microwave radiometer and MMCR | N/A | Microwave radiometer and MMCR | N/A |
| Visibility | Backscatter visibility sensor | Backscatter visibility sensor | N/A | Backscatter visibility sensor |
| Long- and short-wave radiation | Broadband pyranometers & pyrgeometers on board and on ice | Broadband pyranometers & pyrgeometers on board and on ice | Broadband pyranometers & pyrgeometers on the ice | Broadband pyranometer & pyrgeometer on board |
| Turbulent fluxes and surface layer stability | Turbulence and profile instruments on the ice | Turbulence and profile instruments on the ice | Turbulence and profile instruments on the ice | N/A ^b |

^a Number of soundings included.

^b Insufficient sample length.

2.2 Previous expeditions

Data from three other expeditions are used to place ASCOS results into a broader context: the AOE-96, SHEBA and AOE-2001 experiments. ASCOS and the previous *Oden*-based expeditions were of limited length and for different overlapping periods, while SHEBA was deployed for a full year. The overlapping time period for all four expeditions is only 4–23 August, about three weeks; considering only ice-drift components the overlap is even shorter. Directly comparing observations from four different years for such a brief time periods over 12 yr is difficult and likely not even meaningful. For this reason we instead consider the statistics of the different observations, rather than comparing individual time series.

With a primary interest in conditions during late summer and the early transition to autumn, we use all available observations from within the perennial pack ice for the months of July and August from each experiment; while this paper

focuses on ASCOS, we extend the period 1 full day into September to include the end of the ASCOS ice drift. We thus use all available observations made within the perennial pack ice between 00:00 UTC on 1 July and 00:00 UTC on 2 September. A consequence of this strategy is that some of the observations are biased towards the mid-summer melt period (e.g. SHEBA), while other are more dominated by the fall transition (e.g. ASCOS and AOE-96). Figure 2, showing the near-surface temperature records for all four expeditions, illustrates their time overlap. There were also geographical differences. ASCOS, AOE-96 and AOE-2001 were deployed near the North Pole in the North Atlantic sector of the Arctic Ocean, while SHEBA was deployed in the Barents and Chukchi Seas, substantially further south (Fig. 1).

As far as possible we have used the same types of observations to compare different parameters; see Table 1. In some cases data are not available from all expeditions and then the missing expedition is simply omitted from the analysis. In other cases, different types of observations or sensors were

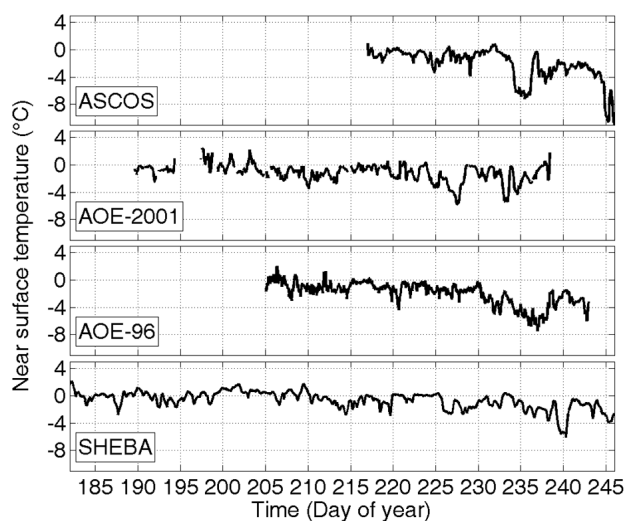


Fig. 2. Near surface temperature ($^{\circ}\text{C}$) time series from the four expeditions, also illustrating the time periods used and the overlap in available data.

used for the same basic purpose. For example, cloud observations in SHEBA and ASCOS were obtained from the MMCR cloud radar while AOE-2001 deployed an S-band cloud and precipitation radar (White et al., 2000) and AOE-96 had no cloud radar. Also, while ASCOS, SHEBA and AOE-2001 had substantial ice drift periods, AOE-96 has only a < 7 day ice drift; data from the latter is omitted. Thus in summary, differences in time, frequency and quality of the observations must be born in mind; it is not the intention of this paper to establish a “summer central Arctic Ocean climatology”.

3 Large-scale atmospheric setting during ASCOS

Figure 3 shows the mean sea-ice area cover for August of each experimental year, from the National Snow and Ice Data Center (NSIDC). The general trend of decreasing summer sea ice extent with time is evident: 1996 had the largest total area cover and 2008 the smallest. There are also interannual differences in the regional location of the pack ice. For example, the ice edge was far north in the Alaskan/East-Siberian sector during 1998 and again in 2008, while being farther south in 1996 and 2001. The ice fraction around the pole was lowest in 1996, consistent with reports of many large open leads during AOE-96 (e.g. Leck et al., 2001), and the local ice fraction was also comparatively low at the SHEBA ice camp. In 2001 total ice cover was a slightly larger and, importantly, the ice fraction was high near the pole, at the location of AOE-2001. Although the ice cover was generally lower again in 2008, especially in the Canada basin, the ice fraction was relatively high at the location of ASCOS.

The synoptic-scale atmospheric circulation exhibits large interannual variability, therefore before examining detailed observations from a limited period it is useful to compare

prevailing conditions to climatology using reanalysis products. Figure 4 shows the main features of the large-scale atmospheric circulation during ASCOS, as manifested by the mean-sea-level pressure (MSLP) and the 850 and 500 hPa geopotential height fields (Fig. 4a–c) and their anomaly, compared to the 1981–2010 climatology for the same time of the year (Fig. 4d–f). The MSLP (Fig. 4a) features high pressure centered over the Canada Basin; there is a separate high-pressure center over Greenland. Low pressure is found over the Barents and Nordic Seas and over the Canadian Archipelago and ASCOS is located roughly on a saddle point. The pressure pattern over the Arctic Ocean is anomalous (Fig. 4d), with a positive anomaly of up to 5–6 hPa over the Canada Basin and a similar negative anomaly over the Barents Sea. This pattern implies an easterly mean surface-flow anomaly over the ASCOS region. The low-pressure anomaly remains at approximately the same horizontal location in the vertical while the high-pressure region moves somewhat westward with altitude (Fig. 4e–f). The anomaly thus exhibits a nearly barotropic character while the pressure-field itself is baroclinic; the low-pressure system tilts north-westward with height.

The region with the lowest temperature tilts with height across the Arctic from the Beaufort Sea region near the surface, centered on the North Pole at 850 hPa and located north of Svalbard at 500 hPa (Fig. 5a–c). The temperature anomaly (Fig. 5d–f) is somewhat similar in the vertical: a dipole pattern with high near-surface temperatures over Greenland and Siberia, with marginally low temperatures on the Canadian side of the Arctic Ocean. A bridge of positive anomalies from Greenland to Siberia strengthens with altitude. Precipitable water (Fig. 6a and c, note the inverted color scale in these plots) is high over Siberia and low over Greenland. The high values over Siberia are anomalous while conditions over Greenland are only marginally moister than climatology. The relative humidity (Fig. 6b and d) is the highest at the surface over the Canada basin, corresponding to climatology, while the anomaly field shows drier than average conditions in a band from north of the Bering Strait along the Siberian coast and to the Kara Sea.

Even though we compare results from ASCOS to three other experiments below, a complete analysis of similarities and differences in the synoptic settings for the four expeditions goes beyond the scope of this paper. However, to provide at least some cursory information on the synoptic scale conditions for the three other experiments Fig. 7 displays the mean and the anomaly MSLP fields for the time period of each experiment, respectively (cf. e.g. Fig. 2). It is clear that ASCOS conditions (Fig. 4a and d) were significantly different; while ASCOS has a surface high-pressure center over the Arctic Ocean with a corresponding low-pressure center over the Barents Sea, all three other experiments have low-pressure centers over the Arctic Ocean, although at different locations. Thus while ASCOS atmospheric circulation was dominated by anticyclonic circulation over much of the

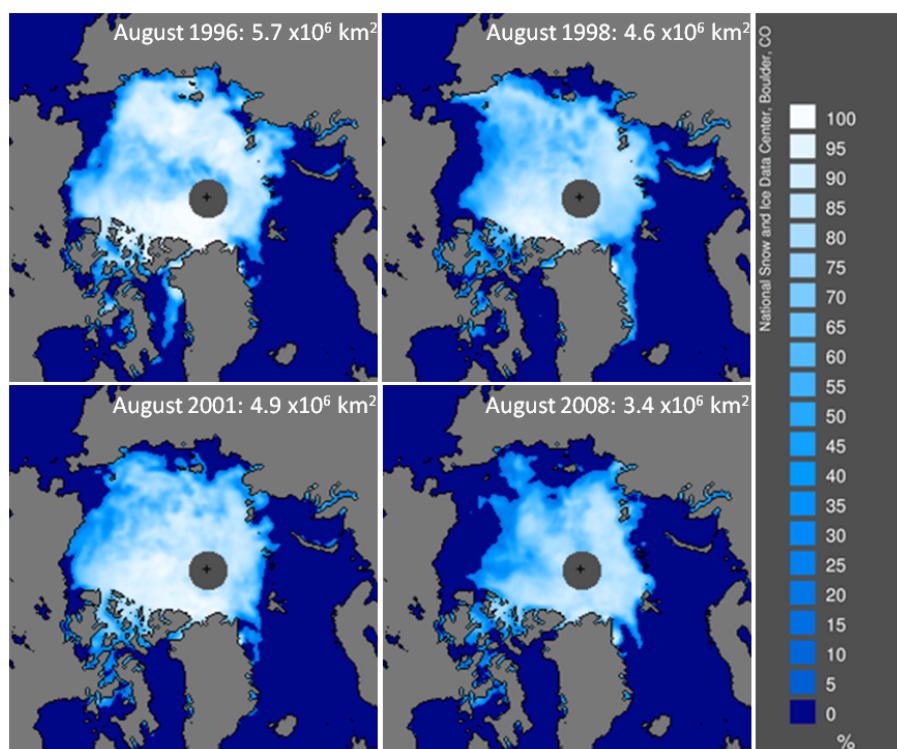


Fig. 3. Mean August sea-ice cover fraction for (a) 1996, (b) 1998, (c) 2001 and (d) 2008, from SSM/I satellite observations. The numbers in the top right of each panel indicate the total sea-ice area, excluding the area around the pole which is not covered by the satellite sensor. The data was obtained from the National Snow and Ice Data Center (NSIDC), Boulder, Colorado.

Arctic Ocean, the other expeditions had cyclonic circulations but with differences in details.

The AOE-96 period had a low-pressure center north of Greenland and eastern Canada, with higher pressure in a band from Alaska around the pole across the Russian Arctic Ocean to Svalbard; much of this pattern is an anomaly. Combining with the AOE-96 cruise track, this locates a large extent of AOE-96 close to a high-pressure anomaly. During the SHEBA summer the low-pressure center was further west, centered on the Chukchi Sea, also with an elongated high-pressure anomaly over the Russian Arctic with a local center over the Barents Sea; the SHEBA ice camp was located on the Bering Sea side of the low-pressure center but on average in a local ridge-like perturbation. Finally, during the AOE-2001 the low-pressure center was even further west, over the Siberian side of the Arctic Ocean with a high-pressure centered over northern Greenland extending out over the Greenland Sea; AOE-2001 was deployed between the low- and the high-pressure centers. Thus while the AOE-96, SHEBA and AOE-2001 summers had distinctly different large-scale circulation over the Arctic Ocean compared to ASCOS, all the expedition tracks were located in regions between the mean low- and high-pressure centers, but with more high-pressure influence during AOE-96 and more low-pressure conditions during SHEBA.

To illustrate how the synoptic scale weather developed over time during ASCOS in response to the mean flow-field displayed in Fig. 4, a select set of ECMWF surface-pressure and 10-m wind analyses are shown in Fig. 8; also included are 12-hourly storm tracks for the most significant weather systems derived from ECMWF analyses. During the first part of the expedition several significant storms passed the ASCOS track moving from east to west; the opposite of the usual direction of travel but consistent with the MSLP anomalies (Fig. 4d). Figure 8a shows the first, starting on 4 August (DoY 217) in the Canada basin and moving clockwise around the pole, reaching the Kara Sea by 7 and 8 August (DoY 220 and 221) then crossing over Svalbard on 10 August and passing south of ASCOS on 12 August (DoY 225), the first day of the ASCOS ice drift. This weather system brought strong winds, precipitation and generally adverse conditions for working on the ice and thus slowed down the initial deployment of instrumentation on the ice.

The next weather system (Fig. 8b) appear on 12 August (DoY 225) over the Kara Sea and moved rapidly westwards, passing south of the ASCOS ice drift on 14 and 15 August (DoY 227 and 228) and dissipated north of the Canadian Archipelago. The flow then changed character; two storms passed rapidly north-eastward across the Nordic, Greenland and Kara Seas without affecting ASCOS (Fig. 8b). After this, synoptic-scale activity eased considerably with the formation

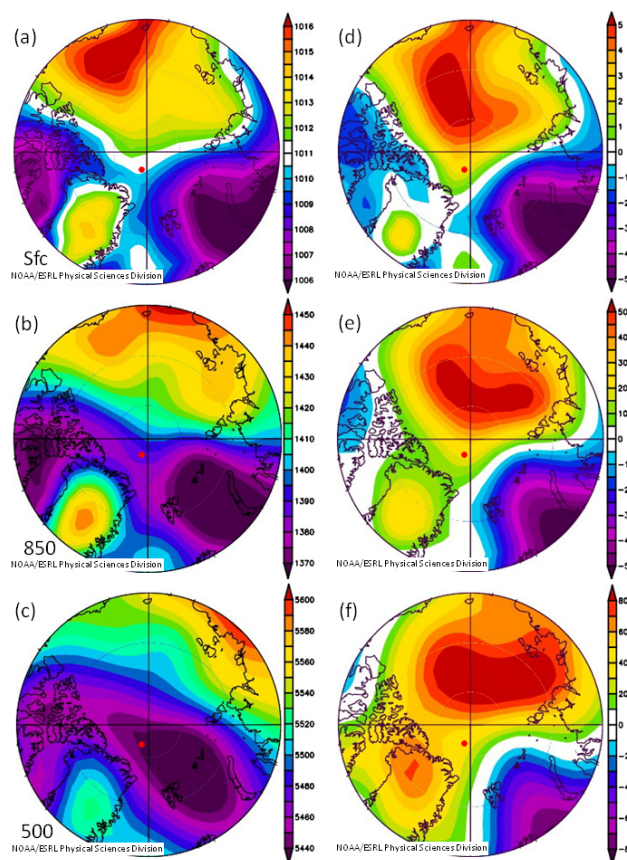


Fig. 4. Contour plots of the (a–c) mean and (d–f) anomaly to climate of mean sea-level pressure and 850 and 500 hPa geopotential height fields for the ASCOS period. The panels show (a, d) mean sea level pressure (hPa) and the (b, e) 850 hPa and (c, f) 500 hPa geopotential heights (m). Images are provided by the NOAA/ESRL Physical Sciences Division, Boulder Colorado from their Web site at <http://www.esrl.noaa.gov/psd/>, and from the NCAR/NCEP re-analysis. Anomalies are calculated with respect to the 1981–2010 mean for the time periods corresponding to ASCOS. The approximate location of the ASCOS ice drift is marked by the red dot.

of a high-pressure system over Svalbard (Fig. 8c) that moved slowly towards and across the North Pole (Fig. 8d). A secondary high pressure over Greenland created a common omega-shaped blocking pattern over the North Atlantic. Towards the end of ASCOS a large intense low-pressure system developed over the Kara Sea and again moved westward towards Svalbard (Fig. 8d) but did not affect ASCOS until after the ice drift was terminated and *Oden* was moving south in the open Greenland Sea towards Longyearbyen.

Figure 9 shows back-trajectories with receptor points at *Oden's* location at 100, 500 and 2000 m above the surface. These heights were selected with cloud processes in mind. The lowest and highest receptor points were designed to be within the boundary layer and in the free troposphere, respectively, while the 500-m level was expected to be roughly in the cloudy layer. Although the

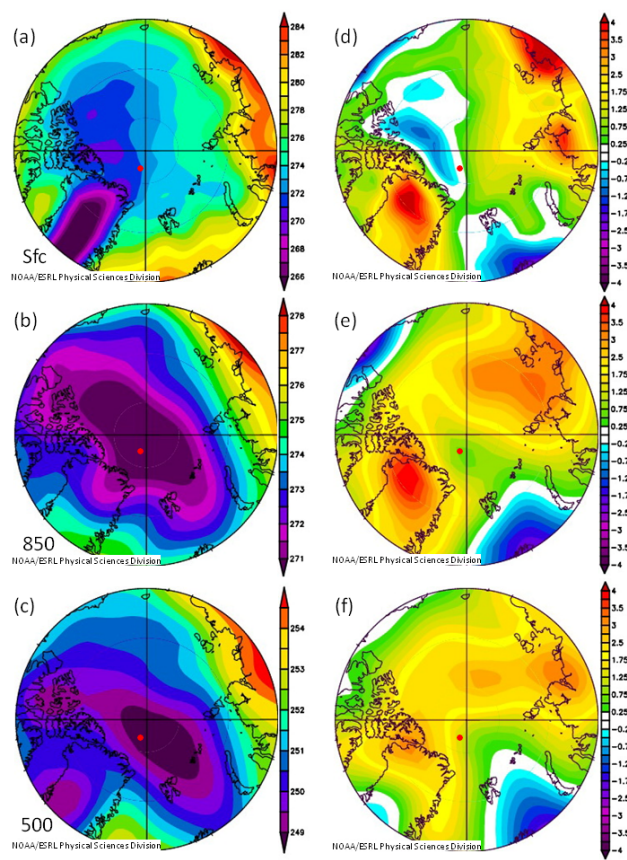


Fig. 5. Same as Fig. 4, but for temperature (K) (a, d) near the surface and at the (b, e) 850 and (c, f) 500 hPa pressure surfaces.

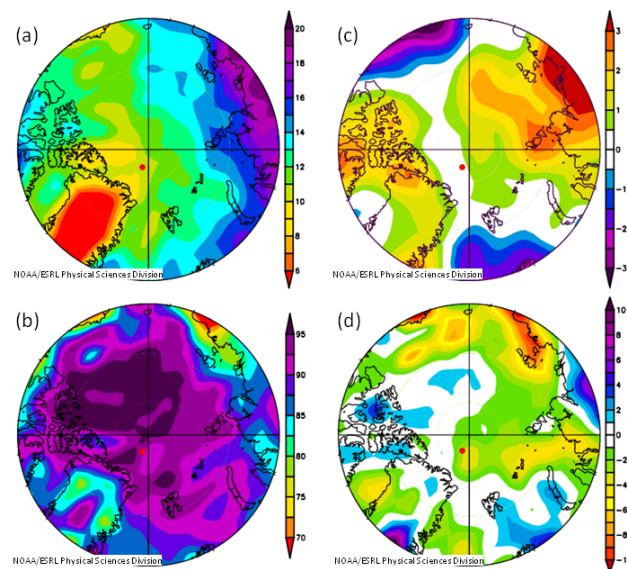


Fig. 6. Same as Fig. 4, but for (a, c) precipitable water (kg m^{-2}) and (b, d) near-surface relative humidity (%).

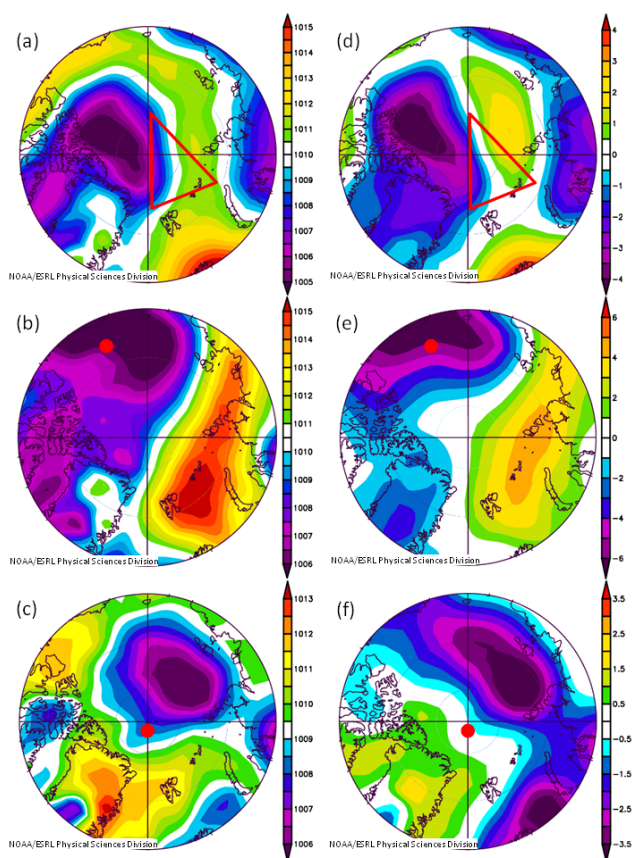


Fig. 7. Same as Fig. 4, but for the (a–c) mean sea-level pressure and (d–f) its anomaly (hPa) for the (a, d) AOE-96, (b, e) SHEBA and (c, f) AOE-2001 field experiments. Red dots/line mark the approximate main locations of the experiments.

variability is large, five broad flow regimes are outlined in the figure. Early, while *Oden* was moving north towards and into the ice (4–9 August; DoY 217–222), the air predominantly arrived from the ice-covered regions north of Canada and Alaska. During 9–20 August (DoY 222–233) the flow-pattern shifted and although highly variable on a daily time scale, air mostly originated from the Greenland, Barents and Kara Seas; this was the synoptically very active period discussed above (see Fig. 8a and b). A new shift occurred around 20 August (DoY 233); trajectories reaching ASCOS then mostly originated in the vicinity of Greenland. Through the end of the ice drift and the beginning of the traverse back to the Greenland Sea (28 August–4 September; DoY 241–248) the origin of the air swings clockwise to come from across the central Arctic. At the end of ASCOS (DoY 248–251), the origin of the air was again from the Kara Sea and adjacent land.

To complement these static pictures, Fig. 10 shows time-height cross-sections of the MMCR cloud radar reflectiv-

ity (Fig. 10a) and the equivalent potential temperature², Θ_e , from the soundings (Fig. 10b) overlaid by subjectively analyzed frontal zones. The latter are identified from the time-rate-of-change of Θ_e , aided by frontal clouds from the MMCR cloud reflectivity; the higher temporal resolution of the radar was used to modify details of the fronts. The type of front is determined from the slope of the Θ_e -gradients with height; warm fronts slope backward with time as the warm air aloft is observed aloft earlier than at the surface, and the opposite for the cold fronts. The most intensive period of weather systems is roughly from 6 through 21 August (DoY 219–234, cf. e.g. Fig. 9). The most significant set of fronts were associated with the synoptic scale disturbance that arrived at ASCOS on the night between 12 and 13 August (DoY 225–226). This active period ended on 20 August (DoY 233), and was followed by a two day period with only low-level cloud or fog that ended on 23 August (DoY 236) with another weather system. Thereafter follows a more quiescent period through 3 September (DoY 236–247), under the influence of the high-pressure system, see Fig. 8c and d), but with several embedded weak frontal passages. These were favorable conditions for a persistent stratocumulus layer residing in the subsidence inversion; note how changes in cloud-top height are associated with the very weak disturbances. Following this, synoptically more active weather reappears as ASCOS nears its end. The conditions observed during the ice drift, outlined by the thick dashed lines, will be discussed in detail in Sect. 5.

4 Meteorological conditions encountered during ASCOS

4.1 Basic meteorological variables

Near-surface temperature during July (DoY 183–213, Fig. 2) remains close to 0°C, as expected for the melt season when all excess heating contributes to melting of ice and snow rather than to a surface warming. Through August (DoY 212–243) all four time series show a very gradual decrease in temperature with time but also feature occurrences of brief colder periods, each lasting for up to a few days. This appears to be a common feature, perhaps signaling the oncoming transition to fall freeze-up conditions, and during AOE-2001 this was associated with breaks or reductions in cloud cover (Tjernström, 2005; Sedlar et al., 2011).

² $\Theta_e = \Theta + \frac{L\Theta}{C_p T} q$, where Θ is the potential temperature defined as $\Theta = T (p/1000)^{\frac{R_d}{C_p}}$, T is the temperature, p is the pressure, R_d and c_p are the gas constant and heat capacity of dry air, respectively, L is the latent heat of vaporization and q is the specific humidity. Note that in the definition of Θ_e for unsaturated conditions, the temperature (T) is evaluated at the lifting condensation level.

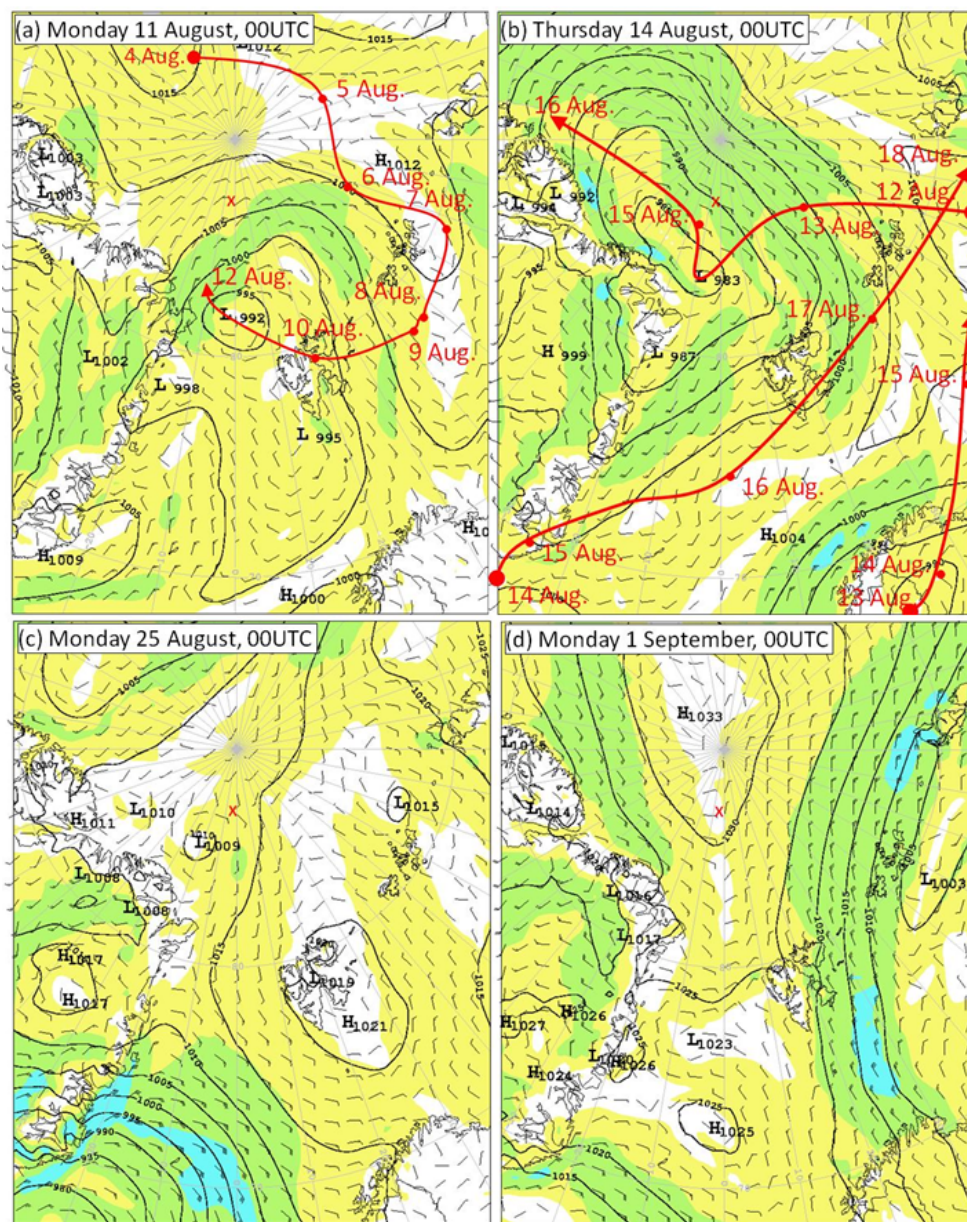


Fig. 8. Sea-level pressure and near-surface wind analyzes for four days during ASCOS: (a) 11, (b) 14, (c) 25 August and (d) 1 September, 2008. Panels (a) and (b) also shows the storm tracks for the major low-pressure centers encountered early during ASCOS with location for the 00:00 UTC on days before and after the analyzes. The approximate location of the ASCOS ice drift is marked by the red x. See the text for a discussion.

Figure 11 shows the relative probability of near-surface temperature, relative humidity and wind speed. In generating these statistics from the three *Oden*-based expeditions we used both the ship's weather station and observations made on the ice during the ice-drifts (absent for AOE-96). For SHEBA we used only observations from the mast on the ice (e.g. Persson et al., 2002). The *Oden* weather station was located at ~ 20 m above the ice, while the height of the observations made on the ice varies between the expeditions,

generally in the 5–15 m interval. Temperatures during ASCOS were mostly in the -2 to 0 °C range, roughly the interval between the freezing points of saline (ocean) water and fresh water (snow), typical for the melt season. The ice-drift measurements also clearly reflect the two periods of lower temperatures around DoY 235 and 245.

The results from the other three expeditions are very similar. SHEBA, with the highest temperatures, peaks at a slightly positive values, while AOE-96 was the coolest

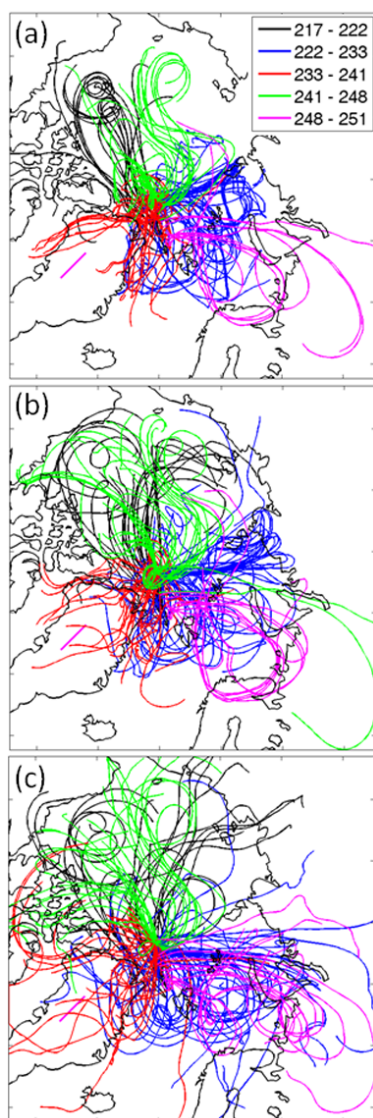


Fig. 9. Five-day back-trajectories calculated from the position of Oden at (a) 2 km, (b) 500 m and (c) 100 m receptor heights. The line colors indicate a rough sub-division into periods with different advection characteristics; see the text for a discussion.

with a broad peak around -1.5°C . All distributions have a pronounced negative tail, SHEBA the least and ASCOS and AOE-96 the most; these are reflections of the temporary drops in temperature that appeared in August. SHEBA's somewhat higher temperatures were likely a consequence of including the whole month of July, which was somewhat warmer on average (see Fig. 2); SHEBA was also at a more southerly location and more solar forcing can be expected (see below). For AOE-96, Leck et al. (2001) report relatively cloud free and cool conditions, and attribute this to a relative lack of positive cloud radiative forcing.

The ASCOS near-surface conditions were very moist (Fig. 11b). The most commonly occurring near-surface rel-

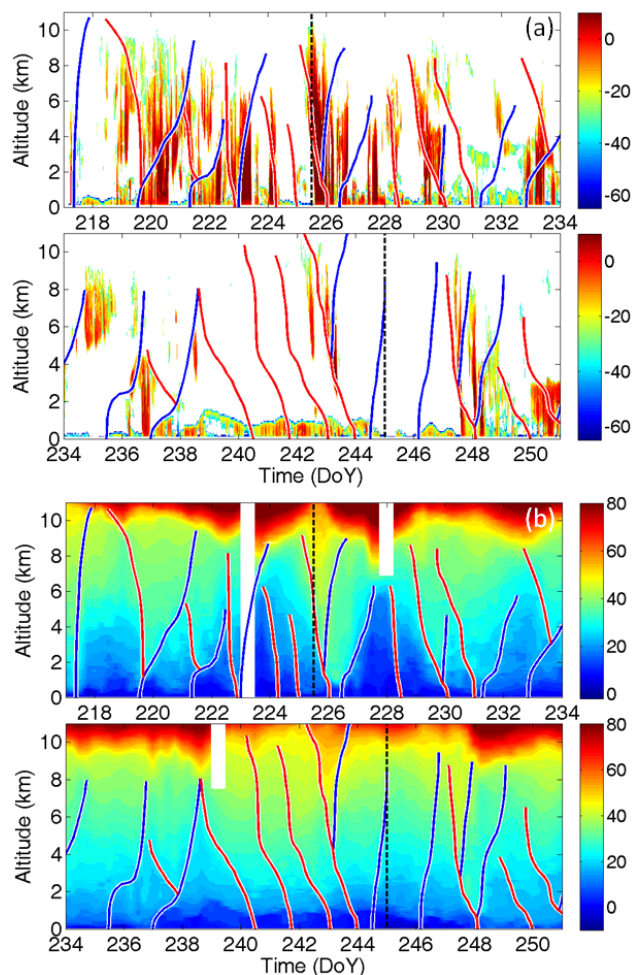


Fig. 10. Time-height cross section of (a) radar reflectivity (dBZ_e) from the MMCR cloud Doppler radar and (b) equivalent potential temperature (Θ_e , in $^{\circ}\text{C}$) from radiosoundings, also indicating subjectively analyzed (red) warm and (blue) cold frontal zones.

ative humidity with respect to liquid (RH_w) was close to 100 % with almost no cases below 90 %. ASCOS conditions falls mid-way between of these expeditions with SHEBA, followed by AOE-2001, being the most humid. AOE-96 was again slightly more different with RH_w peaking at 96 %, consistent with the lower clouds amounts. In terms of relative humidity with respect to ice (RH_i), ASCOS had long periods with high moisture and freezing temperatures that caused RH_i to often be $> 100\%$ (not shown), which during some periods caused substantial deposition of ice crystals on the surface – and on instruments.

The wind speed does not have constraints similar to that for temperature and moisture and is consequently more variable. For ASCOS, the winds during the ice drift were significantly weaker than for the whole expedition (Fig. 11c). The ice drift was relatively more affected by the high-pressure conditions towards the end than the more synoptically active

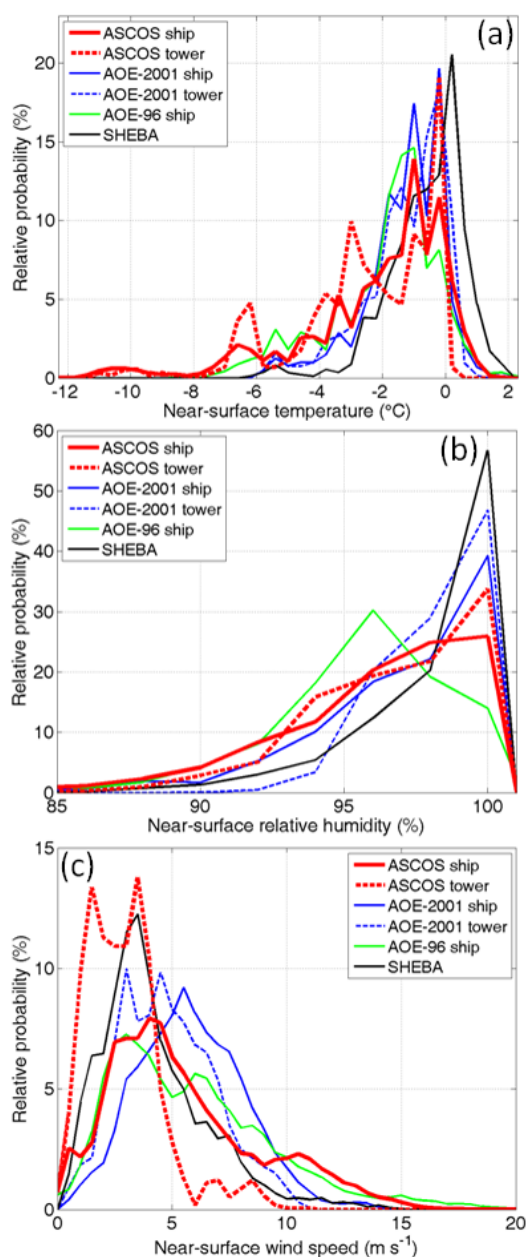


Fig. 11. Near-surface (a) temperature ($^{\circ}\text{C}$), (b) relative humidity (w.r.t liquid, %) and (c) wind speed (m s^{-1}) from the ASCOS, AOE-2001, AOE-96 and SHEBA expeditions.

period at the beginning of the expedition that ended a week into the ice drift. The most common wind speeds for the whole expedition were $3\text{--}5\text{ m s}^{-1}$ with a weak secondary peak at 10 m s^{-1} , and no cases of winds $> 16\text{ m s}^{-1}$. The ice drift was calmer with winds mostly $1\text{--}4\text{ m s}^{-1}$ and very few cases of winds $> 6\text{ m s}^{-1}$. The tower observations from ASCOS, AOE-2001 and SHEBA were made using sensors at a lower height than those made on the icebreaker. A comparison of ship-borne and mast-borne measurements from

ASCOS, only using data from periods when they coexist, suggests that the height of the measurement makes only a small difference for this statistics (not shown). Comparing the expeditions, SHEBA had the lowest winds, while AOE-2001 had the highest, with ASCOS in between. The peak in the AOE-96 statistics is similar to that from SHEBA, but with a secondary peak at higher wind speeds. In general, across all the expeditions, wind speeds were commonly $2\text{--}8\text{ m s}^{-1}$, seldom above 10 m s^{-1} and hardly ever exceeding 14 m s^{-1} .

4.2 Vertical structure

The vertical thermodynamic structure of the lower atmosphere ($< 4\text{ km}$) is evaluated from the radiosoundings. Figure 12 shows the probability of equivalent potential temperature, Θ_e , as a function of altitude. A constant value with height signifies near-neutral moist-static stability conditions, while increasing values are statically stable. Figure 13 shows similar statistics for relative humidity, RH_w .

A dominating feature from ASCOS was a pronounced near-neutrally stratified and very moist layer in the lowest atmosphere. The near-neutral layer extended from the surface up to $\sim 500\text{ m}$ (Fig. 12a) while $\text{RH}_w > 95\%$ persisted in a layer from the surface up to about 1 km (Fig. 13a). With a constantly high RH_w in a deep layer as temperature increases into the capping inversion, it follows that specific moisture must increase with height. This is consistent with results from other studies that specific humidity often increases across the boundary-layer inversion in the Arctic (Tjernström et al., 2004a; Tjernström, 2005; Devasthale et al., 2011; Sedlar et al., 2012). The vertical structure from the three other experiments is strikingly similar to ASCOS, although details differ. The depth of the near-neutrally stratified layer ranged from $300\text{--}400\text{ m}$ in AOE-2001 and AOE-96, to $\sim 400\text{ m}$ during SHEBA (Fig. 12b–d); ASCOS thus featured the deepest neutrally stratified layer. The ASCOS (Fig. 12a) well-mixed near-surface layers appeared preferentially at two temperatures, at $\Theta_e \sim 9^{\circ}\text{C}$ and $\sim 3^{\circ}\text{C}$. A similar feature, although weaker, was present also in AOE-96 (Fig. 12c). In both cases the colder structures were shallower but were still well-mixed. During AOE-96 and SHEBA the boundary-layer Θ_e was slightly lower, at $\Theta_e \sim 7\text{--}8^{\circ}\text{C}$. All expeditions had very high RH_w in the lowest troposphere ($> 95\%$), the highest during SHEBA (Fig. 13d) and the lowest during AOE-2001 (Fig. 13b). The moist layer was also deeper than the well-mixed layer for all expeditions, often reaching to $> 1\text{ km}$. SHEBA had the deepest moist layer, slightly deeper than ASCOS, while AOE-96 had the shallowest layer, $\sim 500\text{ m}$.

This structure, a well-mixed moist boundary-layer with high moisture penetrating the lower inversion, suggests that boundary-layer clouds may more easily detrain into or form in the lower inversion, rather than being capped by it as for example in sub-tropical stratocumulus. Entrainment also becomes a source of boundary-layer moisture. Cloud tops

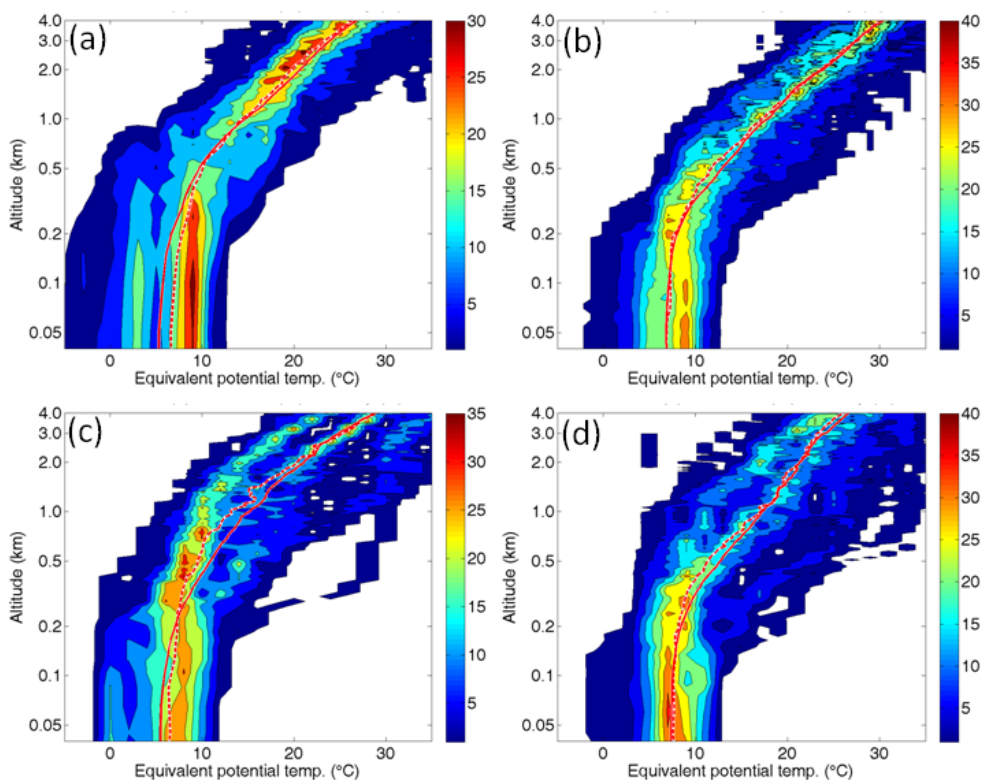


Fig. 12. Probability of equivalent potential temperature (Θ_e , in $^{\circ}\text{C}$) as a function of altitude (km) from (a) ASCOS, (b) AOE-2001, (c) AOE-96 and (d) SHEBA radiosoundings. Solid and dashed red lines are the mean and median profiles, respectively.

penetrating into the lower inversion have been found to be a dominating feature in many Arctic observations, for example from cloud radar and temperature profiles from AOE-2001, ASCOS, SHEBA and at Barrow, Alaska, (Sedlar and Tjernström, 2009; Sedlar et al., 2012) and have been suggested as important for the persistence of Arctic mixed-phase stratocumulus clouds (Solomon et al., 2011).

The characteristics of the main capping inversion are illustrated in Fig. 14, showing statistics for the height to the base of the capping inversion, and its thickness, total temperature jump and static stability. This analysis is based on scanning radiometer temperature profiles from ASCOS and AOE-2001 and on radiosoundings for SHEBA. AOE-96 is omitted due to a relatively low number of soundings. The objective algorithm applied to the temperature profiles to determine the inversions is that of Tjernström and Graversen (2009); the main inversion is defined as that with the strongest local stability; there is a high correlation between strength, stability and depth (not shown). Note that with the data from the scanning radiometer, inversions with a base below but a top above 1.2 km (the maximum height of the scanning radiometer) will be represented in the inversion base statistics, but not in the statistics for thickness, strength and stability.

Over 95 % of all analyzed profiles featured at least one main inversion (cf. e.g. Tjernström, 2005, 2007; Tjernström and Graversen, 2009) and multiple inversions in the lowest kilometer were common. The absolute peak in the probability for the height to base of the main inversion (Fig. 14a) is at ~ 100 m in ASCOS, however, the probability function is fairly flat over the rest of the altitude interval, indicating that high as well as low inversions occurred at similar frequency. The thickness of ASCOS inversions were often around 100–300 m, and the distribution of inversion strengths is broad, $\Delta T \sim 1\text{--}6^{\circ}\text{C}$. Comparing to the other expeditions, both SHEBA and AOE-2001 have more distinct low-level peaks in the inversion base height statistics, with AOE-2001 somewhat higher, at ~ 200 m, and SHEBA slightly lower, more comparable to ASCOS. In neither were there significant occurrences of main inversion bases above ~ 800 m. SHEBA and AOE-2001 had a higher occurrence of thicker inversions, with a broader peak, 100–600 m (Fig. 14b). While AOE-2001 had significantly more weak inversions, with a pronounced peak at $\Delta T \sim 1^{\circ}\text{C}$ (Fig. 14c), SHEBA had similar inversion strengths as ASCOS and inversions never exceed $\Delta T \sim 12^{\circ}\text{C}$ in any of the expeditions. In terms of stability, combining the strength and depth for the individual inversions (Fig. 14d), ASCOS and SHEBA were very similar,

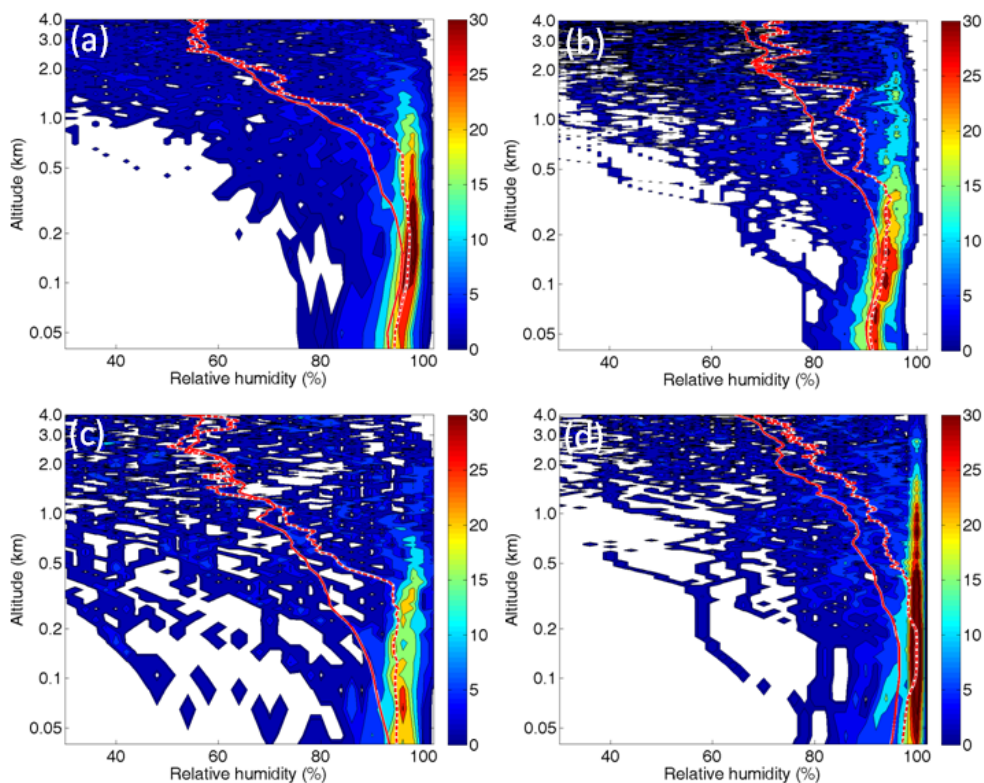


Fig. 13. Same as Fig. 12, but for relative humidity (%).

while AOE-2001 inversions had systematically weaker stability.

Vihma et al. (2008) report on tethered soundings during Tara with similar inversion base heights, ~ 70 m; they report only the mean profile and for a different time, mid-April to late August, 2007. Inversion bases from the Siberian region in Serreze et al. (1992) were substantially higher, at about 300 m, and similar values were also reported in Kahl et al. (1996) using observations from a larger area, including the central Arctic Ocean. Inversion thickness from both Tara and the NP-stations were on average around 500 m, which is deeper than from any of the expeditions we consider here, while inversion strengths range from $\Delta T < 1$ °C (Kahl et al., 1996) to $\Delta T \sim 2$ °C (Serreze et al., 1992), broadly consistent with AOE-2001 but lower than from the other expeditions considered here.

Median temperature profiles from all four expeditions (Fig. 15a) exhibit well-mixed near-surface layers, the deepest from ASCOS and shallowest from AOE-2001, capped by an inversion – strongest and deepest in AOE-2001 and weakest and highest during ASCOS while AOE-96 and SHEBA are very similar. AOE-96 also had slightly higher stability near the surface. Specific humidity (Fig. 15b) varied considerably between the expeditions, the lowest in AOE-96, consistent with subjective reports of less clouds and cooler conditions in AOE-96. SHEBA was moistest, with a signif-

icant layer of higher values between ~ 400 m and ~ 1.2 km. Wind speeds in the lower troposphere, below 1–2 km, were highest during AOE-96 (~ 8 m s $^{-1}$) and the lowest in AOE-2001 (~ 5 m s $^{-1}$) while ASCOS and SHEBA were similar at ~ 6 m s $^{-1}$ (Fig. 15c). AOE-96, and possibly ASCOS, had weak low-level wind speed maxima between 100 m and 1 km indicating the presence of low-level jets; SHEBA and AOE-2001 show no such feature although varying heights, strengths and occurrences of low-level jets may have obscured those in the median profile.

The most striking difference in wind speeds is found in the upper troposphere, where all three *Oden*-based expeditions encountered significantly higher median wind speeds than did SHEBA, at 15–20 m s $^{-1}$ and ~ 10 m s $^{-1}$, respectively, ASCOS having the highest values and AOE-96 the lowest winds. Although this sample is small, the difference may reflect geographical differences in synoptic dynamics. Assuming that wind-speed increase with height across the troposphere can be viewed as a manifestation of baroclinicity instability, these differences might reflect differences in synoptic-scale activity between the two regions, the Beaufort Sea for the SHEBA deployment and the Atlantic sector of the central Arctic Ocean for the *Oden*-based expeditions, and also differences between the years in the latter. The maximum-growth coefficient for baroclinically unstable disturbances, $\sigma = 0.31 \frac{f_0 \Delta}{N}$, was calculated from Eady

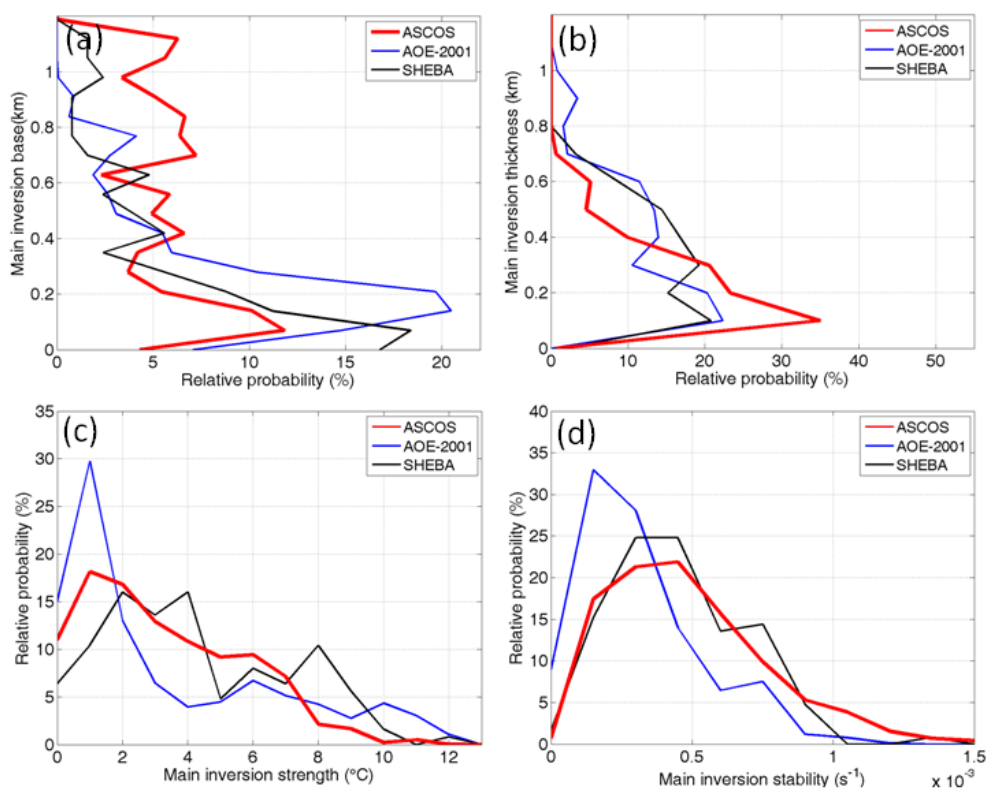


Fig. 14. Inversion statistics showing (a) the height to the base and (b) the thickness (km), and (c) strength (°C) and (d) stability (Brunt Viasalla frequency, s⁻¹) of the main inversion from the (red) ASCOS, (blue) AOE-2001 and (black) SHEBA experiments. See the text for definitions and discussion.

theory (e.g. Holton, 1992), showing the weakest instability for SHEBA, at $\sigma = 0.12 \text{ day}^{-1}$, with values for AOE-96, AOE-2001 and ASCOS of $\sigma = 0.57, 0.67$ and 0.76 day^{-1} , respectively. Here f_0 is the Coriolis force at the approximate latitudes of the expeditions and N , the Brunt-Vaisalla frequency, and Λ , wind shear across the troposphere, are calculated from linear fits to the median potential temperature and wind-speed profiles. Obviously, the small sample, differences in location and the large time intervals between projects makes any conclusions from this highly speculative.

4.3 Clouds

For the purpose of this comparison, “a cloud” is defined by the instruments used for detecting it (see discussion in Shupe et al., 2011). For ASCOS and AOE-2001 cloud fractional occurrence was estimated using ceilometer data, while for SHEBA a multi-sensor approach was used, including lidar and cloud radar. With this in mind, ASCOS and AOE-2001 cloud occurrence fractions might be underestimated, especially for higher clouds, since they use only a single sensor with lower sensitivity at higher altitudes. Note also that cloud fraction is defined using zenith-viewing instruments, sensing clouds as a function of time as they pass above, rather than estimating the spatial cloud cover at any given time. Several

studies have indicated large amounts of low-level cloud in the Arctic during summer (e.g. Intrieri et al., 2002a; Wang and Key, 2005; Karlsson and Svensson, 2010). For ASCOS the average total cloud fraction was about 90 %, while the boundary-layer cloud fraction was about 80 % (e.g. Sedlar et al., 2011). During AOE-2001 the average total cloud cover was 85 %, with 80 % for boundary-layer clouds. Shupe et al. (2011) report a mean cloud fraction from 90 % to close to 100 % from SHEBA, for July and August, respectively. Cloud fraction was not estimated objectively for AOE-96.

The cloud base is defined by the lowest indication of a cloud from the ceilometer (or in SHEBA lidar) or the cloud radar, whichever is the highest, while the lowest cloud top is obtained from cloud radar. For SHEBA, only occurrences with single-layer clouds are used. These dominated in August; in July single-layer clouds were still the most common, while more cases with multiple cloud layers occurred (Intrieri et al., 2002a). The height of the lowest cloud base (Fig. 16a) has a pronounced low-level maximum in all four experiments, peaking below 100 m, while the lowest cloud tops (Fig. 16b) usually occur below 1 km, with a maximum between 200 and 800 m for the three *Oden* expeditions. SHEBA additionally has a secondary peak of lowest cloud-top around $\sim 1 \text{ km}$ and also a higher frequency of even

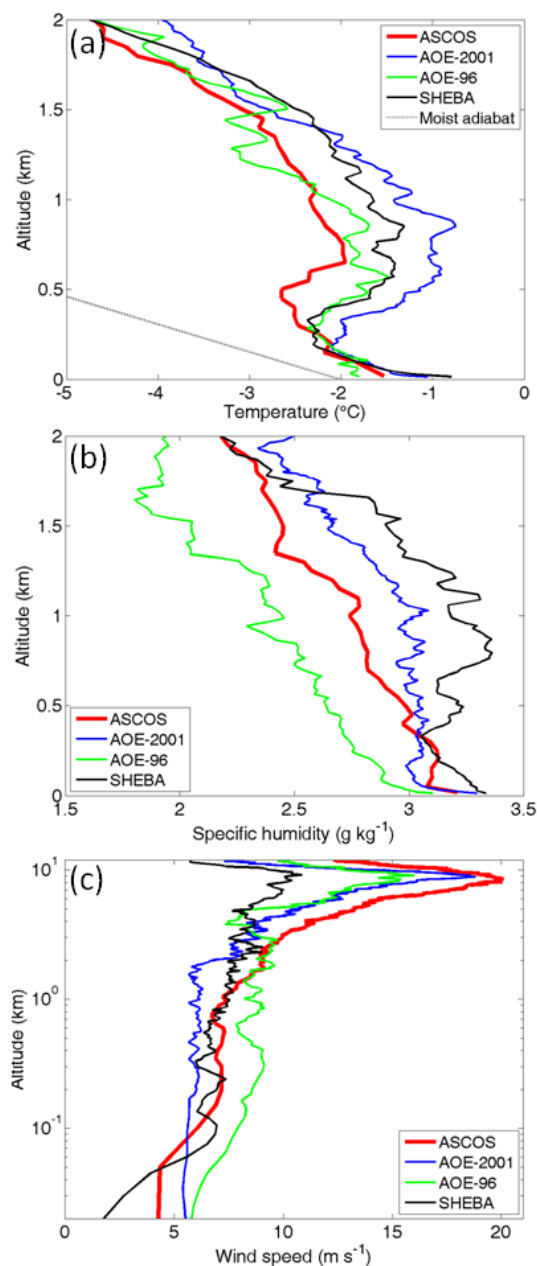


Fig. 15. Median profiles of (a) temperature ($^{\circ}\text{C}$), (b) specific humidity (g kg^{-1}) and (c) wind speed (m s^{-1}) from the ASCOS, AOE-2001, AOE-96 and SHEBA radiosoundings. Note the logarithmic height scale in (c).

higher cloud tops ($> 2\text{--}3$ km). ASCOS and AOE-2001 cloud thickness (Fig. 16c) has a maximum around 300 m, with few clouds thicker than 1 km, while SHEBA has a more uniform distribution between 200 m and ~ 1 km. ASCOS thus had the lowest cloud-bases, AOE-2001 had somewhat shallower clouds and SHEBA, consistent with being more low-pressure influenced (see Fig. 7b), had more deep clouds.

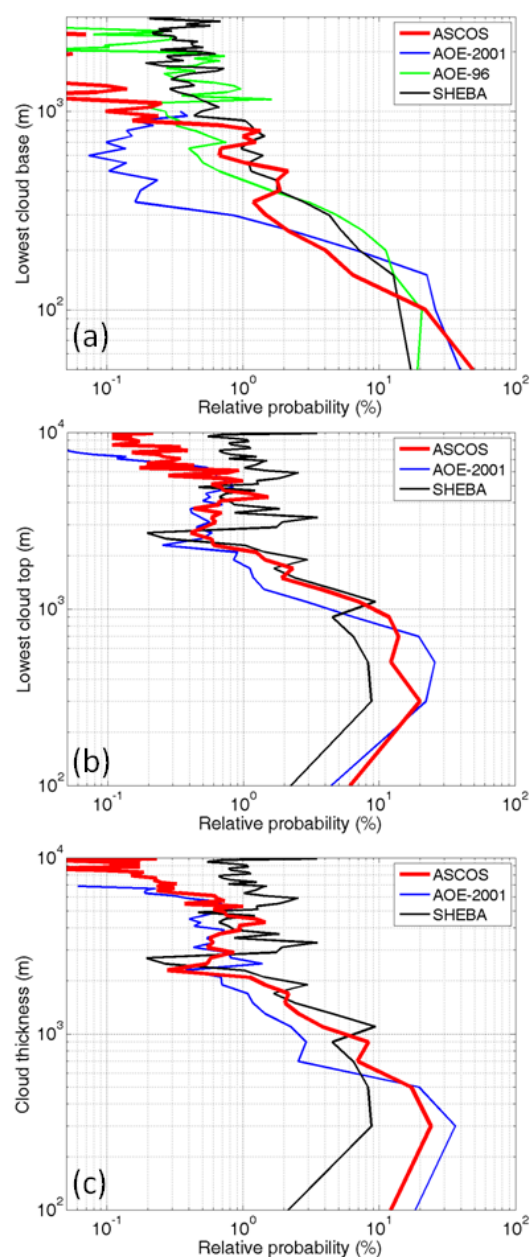


Fig. 16. Probability of (a) lowest cloud base, (b) lowest cloud top and (c) cloud thickness in meters from the ASCOS, AOE-2001, AOE-96 and SHEBA expeditions. Cloud base is estimated from laser ceilometers, while cloud top and thickness is additionally estimated using cloud-radar reflectivity (not available from AOE-96).

ASCOS and SHEBA carried passive dual-wavelength microwave radiometers that continuously monitor vertically-integrated column water vapor (precipitable water) and liquid water path (LWP), the vertically integrated cloud water content (Westwater et al., 2001). Both expeditions also deployed the MMCR cloud radar, facilitating an estimate of cloud ice (Shupe et al., 2005). The total column water vapor

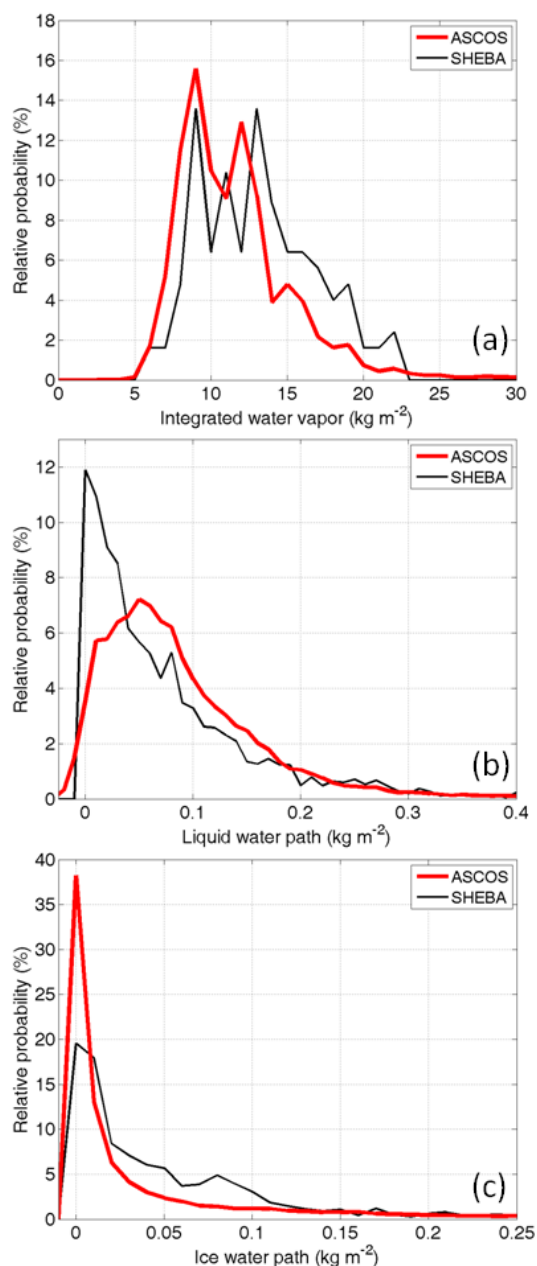


Fig. 17. Probability of total column integrated (a), water vapor, (b) liquid water and (c) ice water paths (kg m^{-2}) from the ASCOS and SHEBA expeditions.

distributions (Fig. 17a) are very similar, with the SHEBA results shifted to somewhat moister conditions, possibly a consequence of SHEBA's more southerly location. In terms of cloud water (Fig. 17b and c), ASCOS had significantly more cloud liquid than SHEBA but less cloud ice.

The three *Oden*-based deployments included visibility observations from a backscatter visibility sensor; for SHEBA this information is not available. All three exhibit similar behavior, with peaks below 1 km (the threshold for fog con-

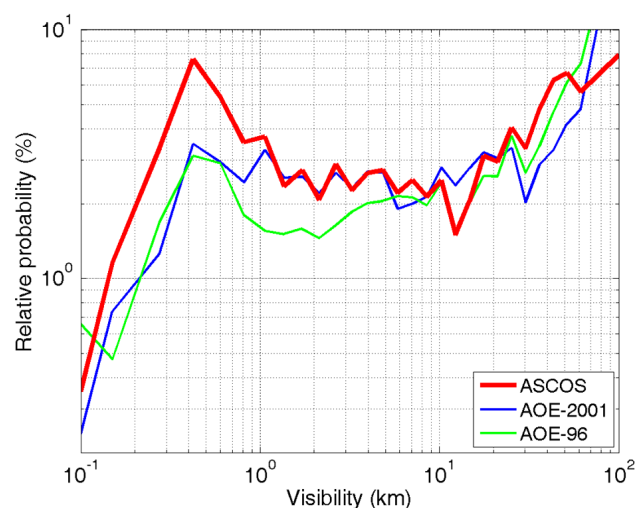


Fig. 18. Probability of visibility (km) from the ASCOS, AOE-2001 and AOE-96, estimated from a backscatter instrument.

ditions according to the WMO definition) and for visibility $> 20\text{--}30$ km (Fig. 18). Note that visibility can be low also in snowfall, when fog is normally dissipated; a backscatter sensor will typically overestimate visibility in snow. Visibility less than 1 km was most common during ASCOS (25 % of the time) and somewhat less during the other expeditions (10–15 %). The relative lack of visibility observations in the 1–10 km range indicates that haze conditions, caused by water uptake on hygroscopic aerosols at $\text{RH} < 100\%$, was essentially non-existent.

4.4 Surface energy fluxes

Incoming (downward) long- and shortwave radiation is strongly affected by clouds and was observed onboard the ship during the three *Oden* expeditions, on the ice during the AOE-2001 and ASCOS ice-drifts, and continuously on the ice during SHEBA. Upward radiative fluxes, and thus net fluxes, are only available from the observations on the ice. ASCOS incoming solar radiation (Fig. 19a) peaks at approximately $50\text{--}100 \text{ W m}^{-2}$, both from the longer ship record and the observations from the ice, while net radiation has a sharp peak at $\sim 10 \text{ W m}^{-2}$. Both incoming and net solar radiation have long positive tails, but with very few values above 200 and 50 W m^{-2} respectively. Incoming longwave radiation (Fig. 19c) peaks around $300\text{--}310 \text{ W m}^{-2}$, with a sharper somewhat lower peak when considering only the ice drift, while the net longwave radiation has a sharp peak at -10 W m^{-2} . Again, both incoming and net radiation distributions have long tails, negative for longwave radiation, down to $200\text{--}220$ and -60 W m^{-2} respectively. This behavior, with distinct peaks and long tails, results from the impact of the clouds. The peaks represent the usually cloudy conditions while the tails, negative for longwave and positive for shortwave, reflect the relatively few clear periods; see Sedlar

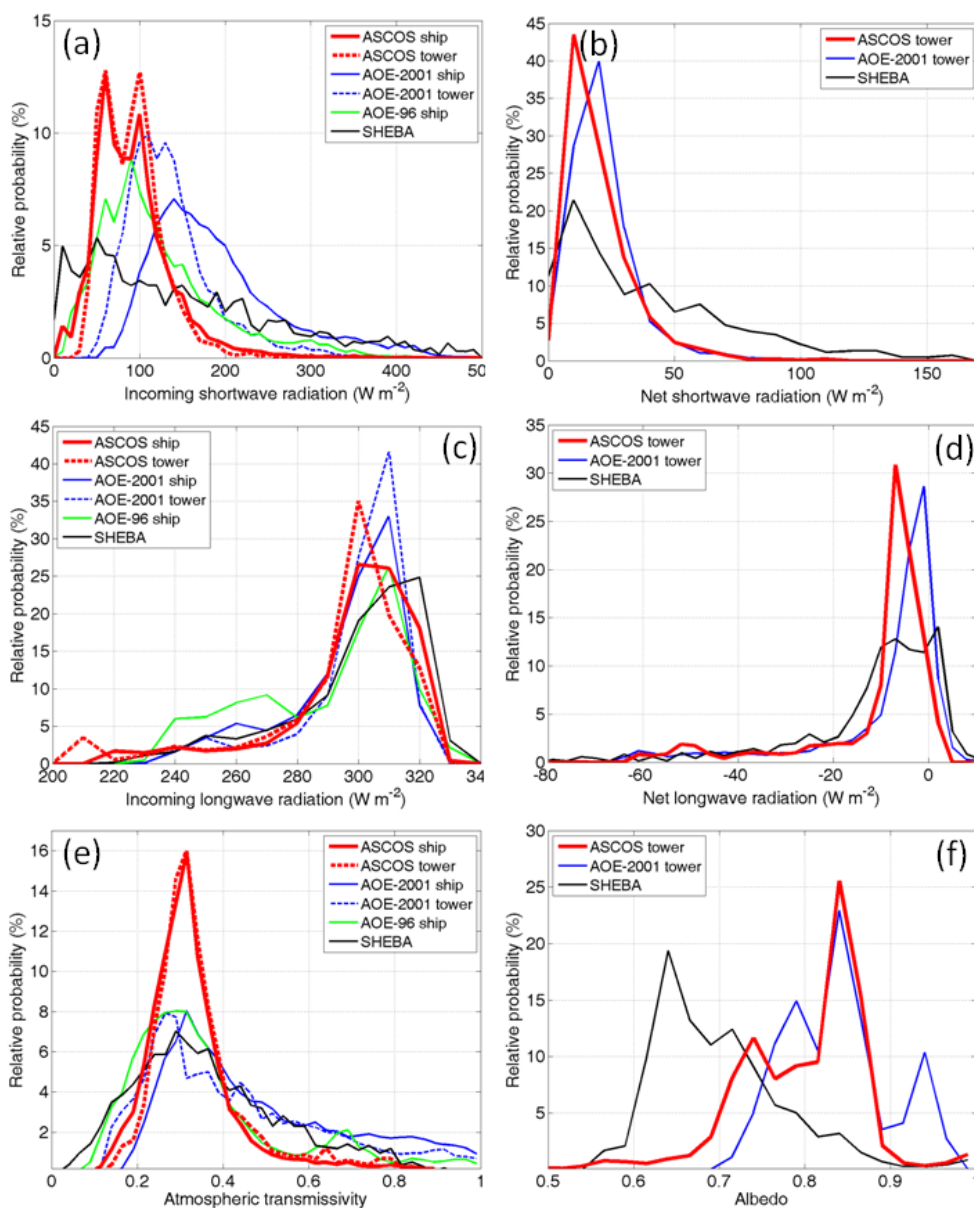


Fig. 19. Probability of (a, c) incoming and (b, d) net, (a, b) shortwave and (c, d) longwave radiation in $W m^{-2}$, and (e) atmospheric transmissivity and (f) surface albedo, from the ASCOS, AOE-2001, AOE-96 and SHEBA expeditions. For ASCOS and AOE-2001 outgoing radiation is only available from the ice-drifts, when instruments were located on the ice, while from AOE-96 net radiation and albedo statistics could not be estimated due to the very short ice drift.

et al. (2011) for a temporal description of radiative fluxes in relation to cloud properties from ASCOS.

Comparing with the other expeditions, there are mainly similarities but also some differences. Incoming solar radiation for the longer ship record at AOE-2001 peaks at $140 W m^{-2}$, while its ice drift probability peaks at slightly lower values, $\sim 100 W m^{-2}$, and the distribution is narrower. AOE-96 has peak values similar to ASCOS, but with a wider distribution, while SHEBA conditions have a much wider distribution with a flat peak around $10\text{--}80 W m^{-2}$

and the longest positive tail. For net shortwave radiation at the surface (Fig. 19b) the distributions from ASCOS and AOE-2001 are similar but with higher peak values for AOE-2001 by about $10 W m^{-2}$; both have similar tails with few values $> 50 W m^{-2}$. SHEBA is again different, peaking at $\sim 10 W m^{-2}$ and exhibiting a broad distribution that tapered off at $> 100 W m^{-2}$.

The incoming longwave radiation (Fig. 19c) was more similar across the four expeditions, with peaks in the $300\text{--}320 W m^{-2}$ range, SHEBA being marginally higher,

while the larger occurrence of lower values in AOE-96 reflects more clear conditions. The same is true also for net longwave (Fig. 19d), with peaks around -10 to 0 W m^{-2} . SHEBA has a somewhat broader distribution and an absolute peak at a few W m^{-2} (positive), and more frequent occurrences of values in the -10 – $(-20) \text{ W m}^{-2}$ range.

The SHEBA shortwave radiation observations stand out. SHEBA was located substantially farther south and from that alone more incoming shortwave radiation may be expected, but also a wider distribution from the fact that zenith angles vary more over the day. But there could also be other systematic differences, for example in the clouds, which could have affected the transmissivity of the atmosphere; for the net radiation also differences in albedo are important. To elaborate on this, we calculated the atmospheric transmissivity and the surface albedo (Fig. 19e and f) for all expeditions. Note here that the albedo was calculated directly from the radiation observations on the masts and is therefore likely higher than a representative surface-area average, which would include open water and melt ponds. Such observations are available only from SHEBA.

All four expeditions have atmospheric transmissivity peaking between 0.2 and 0.4. While ASCOS has a much narrower distribution, to a first order this indicates no major differences in atmospheric transmissivity between the expeditions. Therefore differences in transmission cannot explain for the contrast between SHEBA and the three *Oden* expeditions. Interestingly, the AOE-96 distribution has a secondary peak at 0.65, indicative of occasions with no clouds and a very dry atmosphere. Vihma et al. (2008) calculated mean atmospheric transmissivity to 0.49, 0.46 and 0.56 using data from Tara, SHEBA and NP-stations, respectively; these values are substantially higher than in Fig. 19e. However, the values from Vihma are annual averages; while the NP-station results are in fact consistently higher than the values found here, there is a distinct annual cycle from Tara and SHEBA, with lower transmissivity in late summer when both Tara and SHEBA had values close to our results. SHEBA also had a lower LWP than ASCOS (Fig. 17b) and along with the more southerly location, this contributes to higher incoming shortwave radiation. In addition to a lower LWP, SHEBA also had significantly lower albedo than both AOE-2001 and ASCOS (Fig. 19f), causing additional differences in net shortwave radiation.

Turbulent surface heat fluxes in over the Arctic Ocean sea ice are generally small (e.g. Persson et al., 2002; Tjernström, 2005; Sedlar et al., 2011). In Fig. 20a and b statistics of the turbulent surface energy fluxes for ASCOS are compared to AOE-2001 and SHEBA; upward fluxes are defined positive. The sensible heat flux (Fig. 20a) during the ASCOS ice drift has a sharp peak in probability around zero, with both positive and negative tails. The positive tail is more substantial, to 10 W m^{-2} , while the negative tail down to -5 W m^{-2} is less pronounced. The distributions for the AOE-2001 and SHEBA sensible heat fluxes are quite similar, peaking around

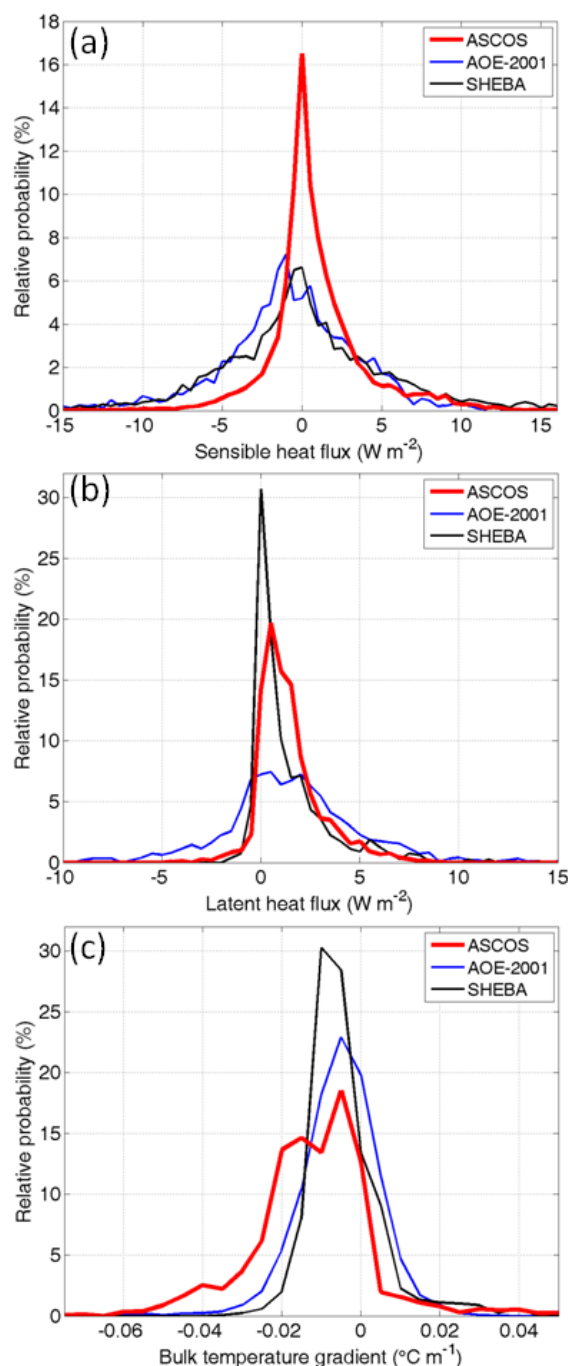


Fig. 20. Probability of (a) sensible and (b) latent heat flux (W m^{-2}), and (c) bulk near-surface temperature gradient ($^{\circ}\text{C m}^{-1}$) from the ASCOS, AOE-2001 and SHEBA expeditions. Turbulent fluxes are calculated from all eddy-correlation measurements within the surface layer ($< 15 \text{ m}$) at each site and defined positive upward. The bulk temperature gradient is calculated as the temperature difference across the mast divided by the vertical distance between the sensors; temperature sensors were located at different heights in the different experiments but in all cases the difference is taken over roughly 8–10 m below a height of 15 m.

zero, and the tails are more pronounced and evenly distributed, $\pm 7\text{--}8\text{ W m}^{-2}$, compared to ASCOS.

The latent heat flux time series have less valid data, because of difficulties in measuring the flux in the Arctic, among other things owing to accumulation of ice frost and riming on the optical surfaces of the open path sensors used in all these experiments. As this would occur mostly in cases with a downward flux of water vapor, exclusion of such episodes may have biased the result. ASCOS and SHEBA fluxes were mostly positive (Fig. 20b) indicating that evaporation is most common, although maximum values are very small, $\sim 5\text{ W m}^{-2}$. AOE-2001 had more cases with a downward latent heat flux, although upward fluxes still dominated. Near zero fluxes dominated during all three expeditions. Figure 20c shows the bulk temperature gradient across meteorological masts, as a simple measure of stability. These are computed over slightly different height intervals, depending on the deployment of the instruments (within 8 to 15 m above the surface). These are relatively similar for all expeditions, with near-neutral conditions being the most common. ASCOS was more frequently unstably stratified than AOE-2001 or SHEBA, consistent with the sensible heat flux (Fig. 20a).

5 Detailed characteristics from the ASCOS ice drift

The ice drift of ASCOS took place roughly between 00:00 UTC 13 August (DoY 225) and 00:00 UTC 2 September (DoY 246), although different instrument systems came on line gradually over the first few days, and the tear-down progressively reduced instrumentation during the last day. The effective length of the ice drift is illustrated in Fig. 21a showing time series of several temperatures near the surface (air temperature at 3.2 m and a set of surface temperatures). Sedlar et al. (2011) analyzed the surface energy budget and defined four main periods for the ice drift with different characteristics; here we refine these definitions and additionally divide the first period into two for a total of five periods, which are discussed below and in Figs. 21–25.

Figure 21a shows that the first two periods were somewhat typical for the melt season. Both had a significant excess of surface energy, as analyzed by Sedlar et al. (2011), that could melt ice and snow at the surface, however, the 1st period was significantly more variable in temperature than the second. Figure 21b shows the cloud radar reflectivity and reveals a more synoptically active 1st period compared to the 2nd, although both were affected by several weather systems as manifested by the deep frontal cloud structures, especially 12–13 and ~ 16 August (DoY 225–226 and 229), with three more minor systems in between. Both periods have a high cloud fraction within the lowest kilometer and also a significant amount of higher cloud, the 1st period more so than the 2nd.

A weather system at the end of the 2nd period (20 August; DoY 233) marks the end of the typical melt-season

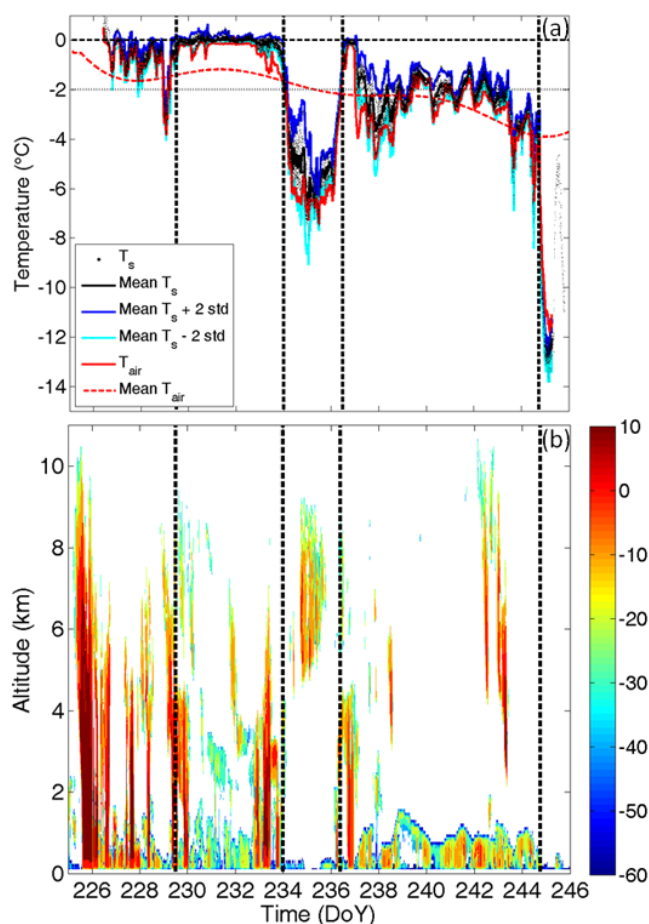


Fig. 21. In (a), time series of 12 individual surface temperature observations (black dots), their mean (solid black), the mean plus and minus two standard deviations, respectively (solid blue and cyan), measured (red) and low-pass filtered (red dashed) near surface air temperature, all in °C. In (b), time-height cross-section of radar reflectivity (dBZ_e) for the ice drift taken from the MMCR cloud radar. Vertical dashed lines show demarcation between the regimes discussed in the text.

conditions and is followed by a 3rd period, which saw mostly low-level clouds and fog and the temperature fell to $\sim -6\text{ °C}$ for approximately 2.5 days (Fig. 21a). Relatively large cloud fractions were associated with this period, although clouds were mostly limited to below 400–500 m. The cloud fraction aloft mostly remained below 30 % with a slight increase around 6–8 km due to the optically thin cirrus cloud seen in Fig. 21b during this period. The surface albedo first increased due to fresh snow from the weather system on the 20th. During the 3rd period, freezing of melt ponds and some of the open ocean, along with heavy riming and frost deposits, increased the surface albedo further (Sedlar et al., 2011). A weather system on 23 August (DoY 236) additionally covered the surface with a layer of new snow. The transmission of solar radiation through the ice also went through an abrupt

change on 24 August (Sedlar et al., 2011; Sirevaag et al., 2011); this also ended the 3rd period. The surface albedo increased from $\sim 70\%$ to $\sim 85\%$ from before to after the 3rd period (not shown) and the surface energy balance did not recover to sustained positive values again.

Surface temperature remained around the freezing point of salt water during the whole 4th period (approximately -2°C , Fig. 21a). This period was characterized by relatively steady conditions, with a significant diurnal cycle in near-surface temperature that now became possible since variations in surface temperature in response to changing heat fluxes were not limited by the melting point of fresh water. Conditions were governed by a quasi-steady high-pressure system (see Fig. 8d), and the dominating feature was a persistent stratocumulus layer. The 4th period thus had a high cloud fraction below 1 km, and approximately 10% cloud cover on average in the free troposphere (Fig. 21b). The lower cloud layers contributed to the maintenance of the surface energy balance close to zero through surface cloud-radiative forcing (Sedlar et al., 2011). As a consequence, the actual transition to the autumn freeze-up was postponed until the end of the 4th period (Fig. 21a). While the height to the top of these clouds was variable in time, towards the end the cloud layer subsided and eventually dissipated around 31 August (DoY 244) at the end of the 4th period. The 5th and final period had a low cloud fraction below 300–400 m and no cloud at all above 1 km, and showed the real onset of the freeze. The surface energy budget became negative (Sedlar et al., 2011) and the temperature rapidly dropped to -12°C , although there was a temporary recovery of the temperature due to reappearing low-level clouds midday on 1st September (DoY 245) (see remaining surface temperature in Fig. 21a, after the mast had been taken down). The ice-drift was terminated at midnight between 1 and 2 September (DoY 246.0) but available ship-borne observations suggest that the surface remained frozen after this (not shown).

Determining the onset of the freeze depends on the definition used. Many studies of different types, using different instrumentation, show a general consensus that the central Arctic Ocean freeze onset often occurs between the 2nd week of August and early September (e.g. Rigor et al., 2000; Belchansky et al., 2004; Overland et al., 2008). One often-used definition is the first time that a running-mean near-surface air temperature falls below differently defined thresholds, e.g. -2°C , to identify the freeze onset. In Fig. 21a the near-surface air temperature, low-pass filtered at a cutoff frequency of two weeks, is shown as the dashed red line. It passes below this threshold at DoY 236 (23 August) consistent with the picture that freeze onset was triggered by the cold 3rd period and solidified by the change in albedo by the snowfall associated with the weather system on DoY 236 (23 August). Note however that the exact timing of -2°C crossing is sensitive to the exact specifications in the low-pass filter design. The actual freeze started almost a week later, when the low-level clouds broke up, allowing the sur-

face to cool rapidly in the longwave (Sedlar et al., 2011). In essence this means that the end of the melt and the beginning of the freeze did not necessarily coincide. Regardless of the definition used and exact date of end-of-melt/freeze-up, it is clear that ASCOS succeeded in capturing this important transition for 2008 during the ice drift.

The thermodynamic vertical structure of the five periods is illustrated by statistics of the profiles of equivalent potential temperature, Θ_e , and relative humidity with respect to ice, RH_i , in Figs. 22 and 23; Figs. 24 and 25 show median profiles of wind speed, and the vertical gradients of Θ_e and scalar wind speed for the five periods, respectively. The first two periods were similar in thermodynamical structure, while slightly different in detail. There was a well-mixed layer at almost 100% relative humidity during the 1st period, reaching to ~ 500 m, while in the 2nd period the well-mixed layer was shallower (to ~ 100 – 200 m) and the moist layer deeper (to ~ 1 km). The wind speeds during the 1st period (Fig. 24) were significantly higher than during any of the other periods, including the 2nd. The temperature gradient from the first period (Fig. 25a) shows a shallow layer of unstable stratification close to the surface, approximately 70 m deep, with a near-neutral but slightly stable layer up to 200–300 m. The wind-speed gradient during this period, although the largest during the ice drift, approaches zero at about ~ 300 m (Fig. 25b). Thus even during the 1st period, which had the most unstable conditions close to the surface and the largest wind shear, the surface-based boundary-layer was limited to about 300 m. The well-mixed layer in the 1st period was topped by a stably stratified layer that extended from about 500 m, up to the capping inversion at about 1 km (Fig. 25a). The 2nd period was slightly more stably stratified close to the surface, near-neutral up to 200 m. Then it became gradually more stable up to ~ 1 km; above this the structure is similar to the 1st period.

The 3rd period, although signified by lower near-surface temperatures, was still well-mixed near the surface, but only in the lowest ~ 50 m. This layer was capped by a strong inversion extending to 400–500 m with free-tropospheric conditions aloft (Figs. 22c and 25a). The corresponding moist layer was ~ 200 m deep and the RH_i in this layer was $> 100\%$ (Fig. 23c) consistent with the formation of frozen drizzle from the low-level clouds and the accumulation of rime and frost on the surface. The wind speed was the lowest during the ice drift (Fig. 24) with an indication of a weak low-level wind-speed maximum around 100–200 m. Consistent with this jet-like feature the wind-speed gradient crossed zero around 150 m and was negative but small up to ~ 300 m (Fig. 25b).

The 4th period had a somewhat deeper and only slightly stable near-neutral layer in the lowest 100 m and then was more stable but still near-neutral in the 200–800 m layer with a capping inversion at ~ 1 km. A clear double structure is visible in both Θ_e and RH_i , with a secondary well-mixed layer ~ 800 – 1000 m (Figs. 22d and 23d). In this double-layer

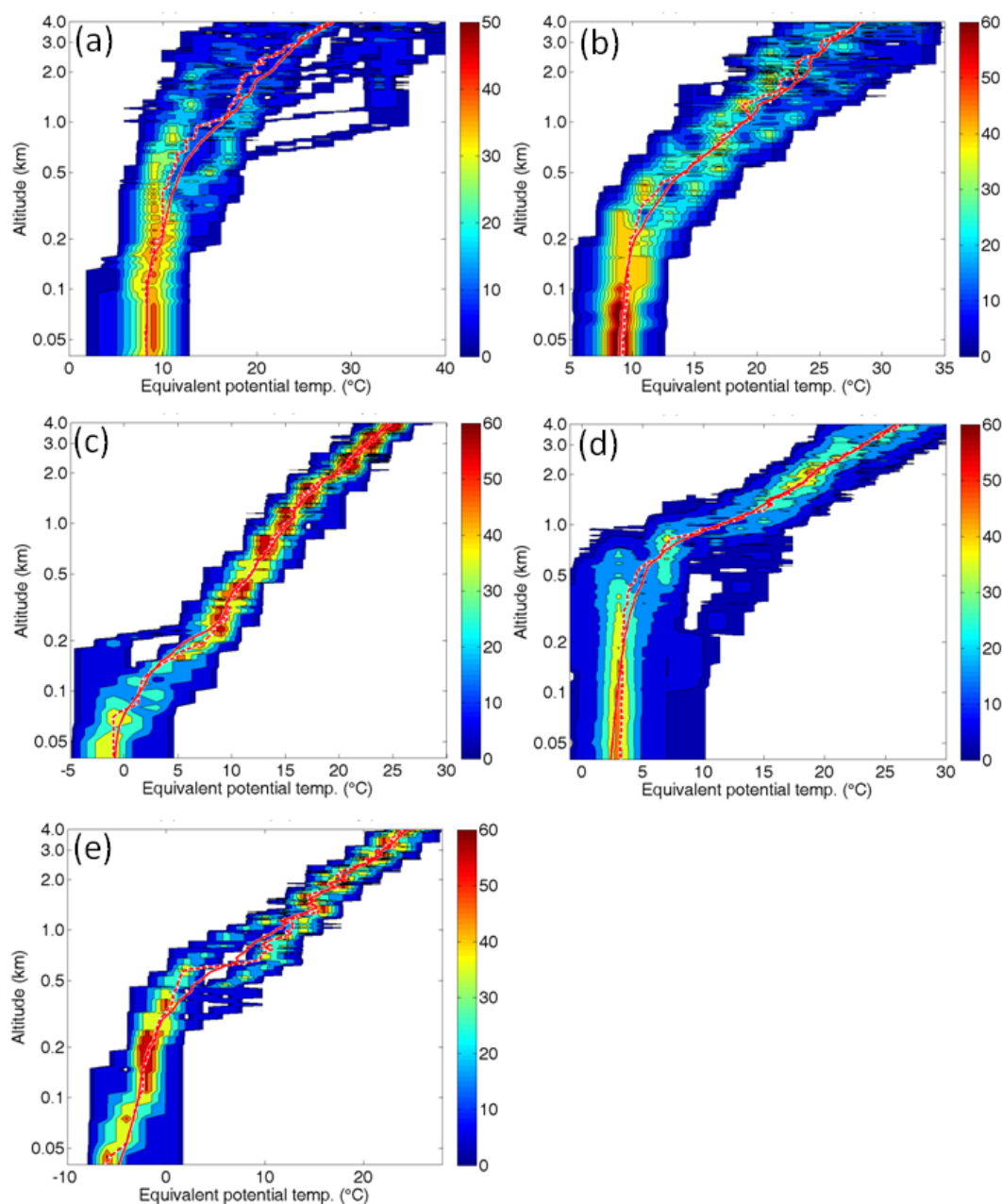


Fig. 22. Same as in Fig. 12 but for the five different periods defined in Fig. 20: (a) 1st, (b) 2nd, (c) 3rd, (d) 4th, (e) 5th periods.

structure RH_i first increased with height in the lowest 200 m followed by a slight minimum and a secondary maximum in the upper layer, well above 100 %. The upper of these well-mixed structures was associated with the stratocumulus cloud layer that was present for most of the 4th period. The average wind shear during this period was zero above 200 m (Fig. 25b).

This period is of special interest with its persistent stratocumulus layer and the deep boundary layer with two distinct well-mixed layers in the thermodynamical structure. Since the upper well-mixed layer was thermodynamically

separated from the near-surface atmosphere and the wind shear goes to zero well below the upper layer, this suggests that the cloud layer was intermittently decoupled from the surface. This indicates the presence of a three-layer structure: (1) a shallow surface-based boundary layer, about ~ 200 m deep on average, where turbulence was predominantly driven by wind-shear; (2) an upper layer associated with the clouds, where turbulence was generated by buoyant overturning driven by cloud-top longwave cooling; (3) in between these two layers there was a second layer with near-neutral characteristics. From previous observations (e.g. Tjernström, 2005),

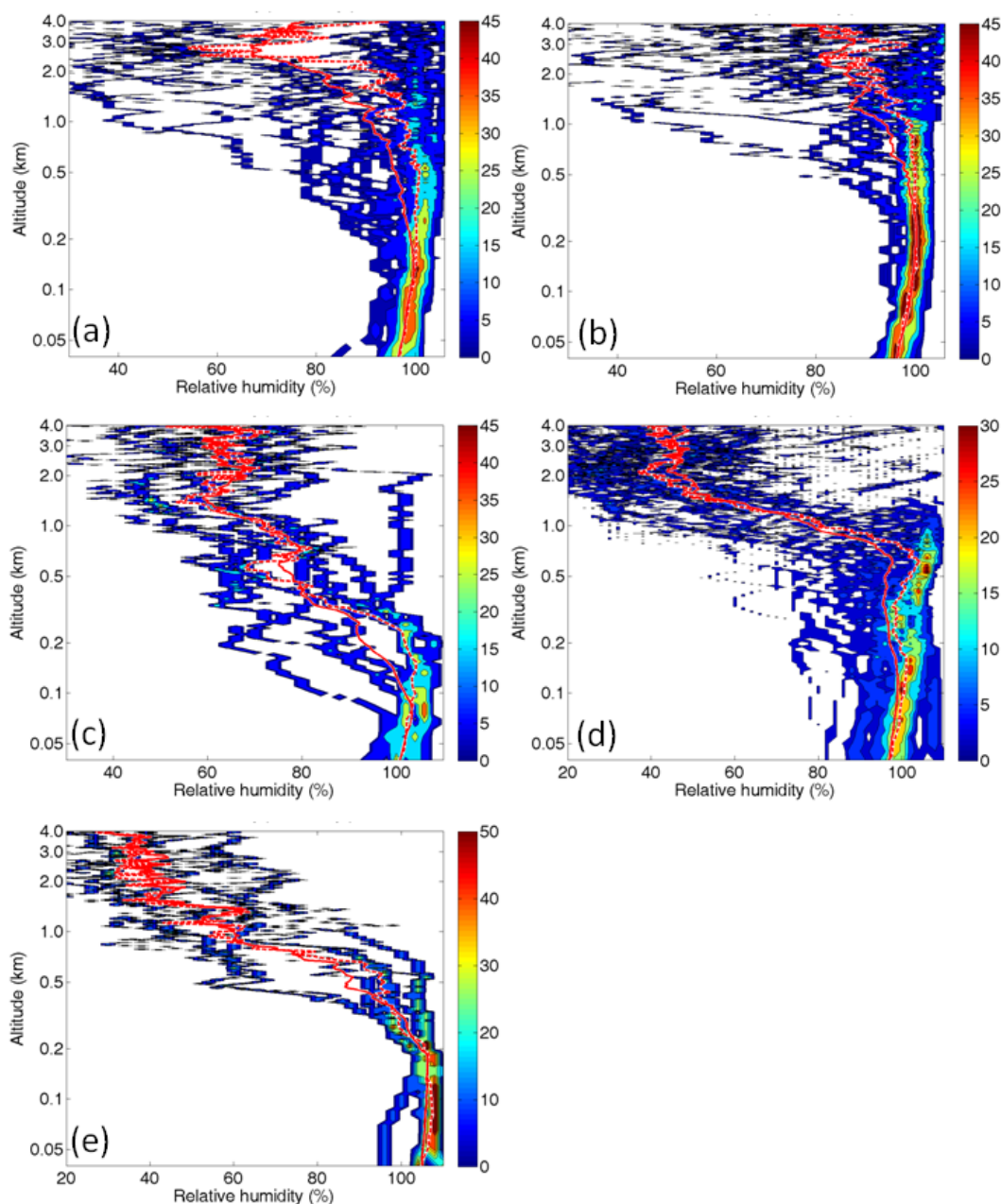


Fig. 23. Same as Fig. 22 but for relative humidity with respect to ice, RH_i (%).

the inversion base statistics in Fig. 14 and the depth of the shear layer in Fig. 25b, it seems unlikely that surface-based turbulence would be able to mix such a deep layer as from the surface and up through the cloud layer. The shear-driven boundary layer is too shallow to sustain the deep well-mixed layer observed in the thermal structure in Fig. 22d. The somewhat lower RH_i in the layer between 200 and 500 m also suggests that this intermediate layer has a different character. This suggests that the surface-based boundary layer is too shallow on its own to connect the surface layer and the stratocumulus layer. The well-mixed upper cloud layer, on the

other hand, is generated by cloud-induced turbulence, from cloud-top cooling. If sufficiently strong this mixing may penetrate downward to the top of the surface based mixed layer. The persistence of the stratocumulus cloud layer during the 4th period, in light of a lack in persistent surface-to-cloud layer mixing, suggests such cloud formation inherently relies upon a moisture source near cloud top in the vicinity of sufficient buoyancy generation from longwave cooling; this picture agrees with the hypotheses and modeling results of Solomon et al. (2011) and Sedlar et al. (2012). The upper and lower layers may then connect and turbulence can couple the

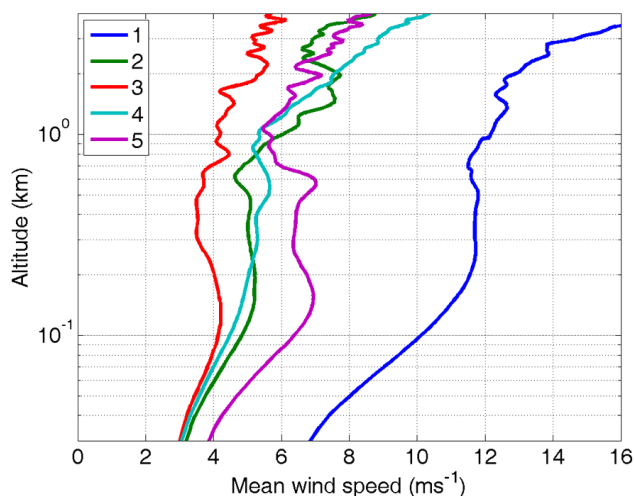


Fig. 24. Median wind-speed profiles (m s^{-1}) for the lowest 4 km, for the five periods defined in Fig. 20 and discussed in the text.

surface and clouds, and transport, for example, moisture or aerosols between these layers. The well-mixed structure imposed on the layer between the top of the lower layer and the cloud layer during such mixing episodes may remain long after the mixing itself has ceased, like in a residual layer.

The 5th and final period displays a strong surface-based inversion up to ~ 100 m, by far the most stably stratified boundary layer during the ice drift, and is capped by a secondary inversion starting at 300 m and transitioning to free tropospheric conditions above 800 m (Figs. 22e and 25b). The second stable layer 300–500 m was likely the remnants of the dissipating subsidence inversion in which the stratocumulus layer was previously residing. As the cloud dissipated, the buoyancy-generated turbulence from the cloud, forced by cloud-top cooling, has dissipated and the layer was becoming increasingly stably stratified. The wind speed in the lowest kilometer increased during the 5th period and is the second strongest during the ice drift (Fig. 24) although the winds aloft are weaker and comparable to periods 2 and 4. The wind shear first approaches zero at around 150 m with a 100 m shallow layer of negative shear on top (Fig. 25a).

6 Summary and conclusions

The Arctic Summer Cloud Ocean Study (ASCOS) was deployed on the Swedish icebreaker *Oden* through most of August and into early September 2008, as part of the International Polar Year. The science focus of ASCOS is on the formation and life-cycle of low-level clouds and their effect on the surface energy budget.

To understand and generalize many of the processes studied during ASCOS, an understanding of the meteorological processes at play is necessary. One objective of this paper is therefore to provide an overview of the meteorological con-

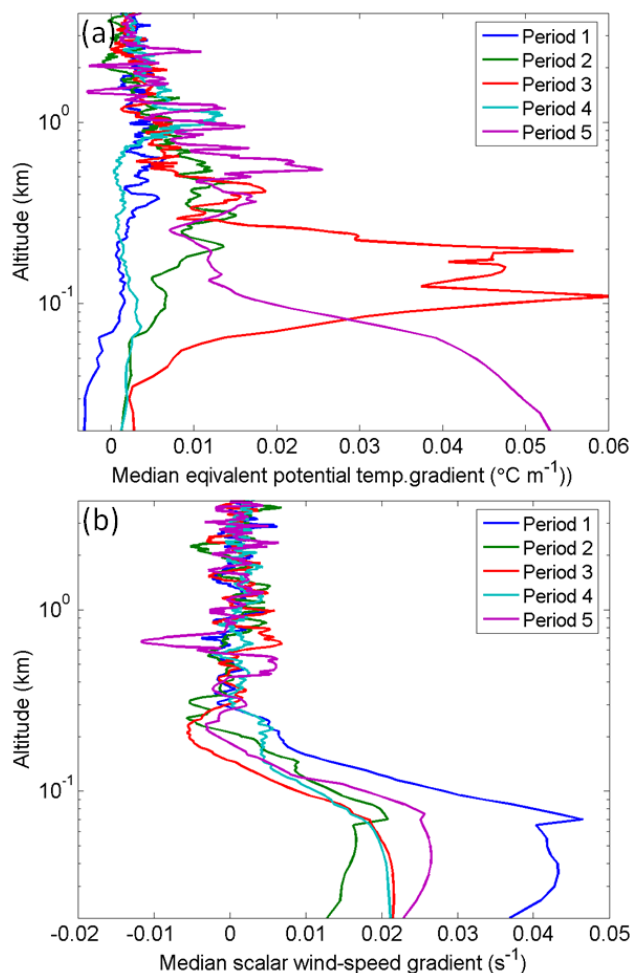


Fig. 25. Same as Fig. 23 but for the vertical gradients of (a) equivalent potential temperature (Θ_e , K m^{-1}) and (b) wind speed (s^{-1}).

ditions that were encountered during ASCOS, in particular during the ice drift. Research-quality observations from the central Arctic Ocean are sparse and often taken over short time periods; interpreting the results requires analysis of the generality of the observations. Thus a second objective of this paper is to compare the meteorological conditions during ASCOS with those from similar previous field studies in the central Arctic Ocean during the summer season: the AOE-96, SHEBA and AOE-2001 expeditions from the summers of 1996, 1998 and 2001, respectively.

The ASCOS time period was characterized by a high-pressure anomaly over the Canada Basin and a low-pressure anomaly over northern Norway into the Barents and Kara Seas. The pressure anomaly had an almost barotropic vertical structure and generated an anticyclonic large-scale flow pattern over the central Arctic Ocean. As a result, several low-pressure systems propagated westward around the pole and across the path of ASCOS in the North-Atlantic sector of the Arctic, especially during the first half of the expedition.

The Siberian continent and Greenland had higher than average temperatures at the surface; aloft these two warm centers joined across the Arctic Ocean in a band of higher than normal temperatures. Over the Siberian Shelf region conditions were moister than average but the ASCOS region was close to climatology in terms of low-level moisture and precipitable water. This large-scale pattern was different to those during the previous expeditions used in this study; all of these had a cyclonic flow-pattern with low-pressure centers over the Arctic Ocean. However, considering the location of the different experiments, the conditions were more similar; all were located between low- and high-pressure centers, albeit with SHEBA having more of a low-pressure influence and AOE-96 being closer to a high-pressure area.

ASCOS was under the influence of significant synoptic-scale activity for the first half of the expedition, up until around 20 August, after which a high-pressure situation dominated until the end of the campaign. Air mass origins for the synoptically active period were mostly from the Kara and Greenland Seas. During the high-pressure dominated period the air mass origin was first from the Greenland region and then gradually shifted over to the Canadian Archipelago and then across the western Arctic Ocean.

In terms of both basic near-surface meteorology and the vertical structure, ASCOS was broadly similar to the previous expeditions analyzed. Near-surface temperature was mostly in the -2 to 0°C interval, with a tail of lower temperatures in the probability distribution reaching around -10°C . This tail is a result of brief colder episodes that start appearing in August in all the expeditions. Conditions were also consistently very moist, with relative humidity mostly $> 90\%$. Near-surface winds were most often in the $2\text{--}8\text{ m s}^{-1}$ range and seldom $> 10\text{ m s}^{-1}$. The cloud fraction was high during all expeditions and was dominated by low-level clouds. The lowest cloud base was most often below 100 m in all four expeditions and the lowest clouds were usually $200\text{--}500\text{ m}$ thick, occasionally reaching 1 km , most often during SHEBA. Visibility indicates frequent fog conditions while visibility outside of fog was usually high, most often $> 20\text{--}30\text{ km}$, even below low-level clouds, indicating an absence of haze. Visibility less than 1 km was most common in ASCOS, at $\sim 25\%$ of the time, while the other two *Oden*-based expeditions had low visibility $10\text{--}15\%$ of the time.

Solar radiation, incoming as well as net, reflected the cloudy conditions, with peaks at ~ 100 and $20\text{--}30\text{ W m}^{-2}$, respectively. Incoming and net longwave surface radiation also reflected the cloudy conditions, with peaks between $300\text{--}320$ and $-10\text{--}0\text{ W m}^{-2}$, respectively. The positive (negative) tail in the net shortwave (longwave) distribution comes from the few cloud free episodes. Turbulent fluxes were in general small, within $\pm 10\text{ W m}^{-2}$; however, as stated by Sedlar et al. (2011), often similar in magnitude to the residual in the surface energy budget, i.e. the heat that remains available for freezing or melting, and are therefore still of importance.

ASCOS, like the other three expeditions, featured a well-mixed and very moist boundary layer, capped by an inversion. The depth of the mixed layer and the height, depth and stability of the main capping inversion were different in the four expeditions, but the basic structure was very similar. Another common feature in all the expeditions was the depth of the layer with high moisture, which often reached well above the top of the well-mixed layer, indicating that specific moisture often increased within the capping inversion, unlike conditions in mid-latitude and sub-tropical boundary layers. This implies that entrainment of air from the free troposphere is often a source of boundary-layer moisture and can act to maintain the high moisture observed near the surface.

The ASCOS ice drift spanned the end-of-melt/freeze onset transition. This transition is related to synoptic-scale meteorology; snowfall from synoptic systems and deposition of frost and rime increased the surface albedo at a time when net energy fluxes at the surface were approaching zero. This altered the surface energy budget sufficiently that surface melt conditions could not reestablish. The transition to colder temperatures after the end of the melt season was delayed almost a week by the presence of a persistent stratocumulus cloud layer that, by its surface radiative forcing, prevented the surface energy balance from becoming negative (Sedlar et al., 2011). In a sense one can say that the start of the real freeze did not coincide with the end of the melt; there was nearly a week-long period in between.

Thus, taking ASCOS together with the previous expeditions, a common picture emerges, with near-surface temperatures near or just below 0°C and very high relative humidity, $> 90\%$ (often $> 100\%$ with respect to ice), large amounts of low-level clouds in a well-mixed shallow boundary layer capped by a weak or moderately strong inversion where high humidity, and sometimes also the cloud top, penetrates well into the inversion, but where the visibility below clouds is often unexpectedly good. The first cloud top is usually below 1 km . This structure was virtually the same across all the expeditions examined in the paper; only the average depths of the well-mixed and the high-moisture layers varied.

The largest difference was found in the shortwave radiation conditions from SHEBA; this difference is attributable to the more southerly location of the SHEBA ice camp and partly also to the lower surface albedo. SHEBA also has somewhat deeper clouds on average, possibly because of the somewhat more low-pressure influenced location during the investigated time period. The results from AOE-96 were slightly cooler and less moist, with somewhat less clouds. This is consistent with a slightly more high-pressure influenced location for much this expedition.

Turbulence in this boundary-layer system is generated at the surface and in the cloud layer. At the surface, turbulence generation is predominantly due to wind shear; although convective conditions occurred the sensible heat flux was always small ($< 10\text{ W m}^{-2}$). This layer is typically shallow, usually some $100\text{--}200\text{ m}$ deep, except during a few high-wind

periods. In the cloud layer, turbulence is produced by buoyancy driven by cloud-top radiative cooling. This process is independent of the surface and the layered boundary-layer structure may be understood in terms of the relative importance of these two processes. If the cloud layer is low enough or the cloud-generated turbulence strong enough, the mixing may reach well below the cloud base and even into the surface-based mixed layer. If, on the other hand, the clouds are sufficiently elevated or the cloud-induced turbulence is weaker, the layers will be separated. Sedlar et al. (2012) showed that a redistribution of some cloud liquid water above the inversion base impacts the longwave radiative cooling of the cloud layer, and thus alter the overturning buoyant motions driven by the cloud. The vertical structure encountered during ASCOS, especially during the 4th stratocumulus-dominated period of the ice drift may be a reflection of this, with its apparent three-layer structure, where the well-mixed middle layer may be a reflection of the sporadic coupling of the layers. This would explain the deep well-mixed structure, which is substantially deeper than the wind-shear layer. Much of the boundary-layer mixing is probably due to cloud-top cooling and subsequent buoyant overturning of the cloud, implying a connection between the clouds and the free troposphere due to entrainment at the cloud top. This was probably even more the case during AOE-2001 when the cloud- and surface-layer turbulence was more coupled (see Tjernström, 2007). These processes and how they interact should be the focus of more study, experimental as well as with modeling.

Acknowledgements. This work is part of the Arctic Summer Cloud-Ocean Study (ASCOS). ASCOS was an IPY project under the AICIA-IPY umbrella and an endorsed SOLAS project. ASCOS was made possible by funding from the Knut and Alice Wallenberg Foundation, the DAMOCLES Integrated Research Project from the European Union 6th Framework Program and the Swedish National Research Council (VR) while the Swedish Polar Research Secretariat provided access to the icebreaker *Oden* and logistical support. Support from the US National Science Foundation (NSF) and the National Atmospheric and Oceanic Administration for the remote sensing instruments for the cloud observations and from the UK Natural Environment Research Council (NERC) for some of the surface exchange and boundary-layer observations is gratefully acknowledged. MT, CL, TM and JS were also funded by VR, DAMOCLES and the Bert Bolin Center for Climate Research at Stockholm University, IMB and CEB were funded by NERC while MDS, POGP, CRW and MS were funded by the NSF. CEB was additionally funded by the UK Met Office, while JP was supported by the Academy of Finland, the Finnish Academy of Science and the Letters/Vilho, Yrjö and Kalle Väisälä Foundation. We are grateful to the science teams from AOE-96, SHEBA and AOE-2001 for supplying data. Finally we are indebted to the *Oden's* Captain Mattias Peterson and his crew for invaluable assistance with many things during the field deployment of ASCOS.

Edited by: J. W. Bottenheim

References

- ACIA: Impacts of a warming Arctic: Arctic Climate Impact Assessment, Cambridge University Press, 2005.
- Belchansky, G. I., Douglas, D. C., and Platonov, N. G.: Duration of the Arctic sea ice melt season: regional and interannual variability, 1979–2001, *J. Climate*, 17, 67–80, 2004.
- Birch, C. E., Brooks, I. M., Tjernström, M., Shupe, M. D., Mauritsen, T., Sedlar, J., Lock, A. P., Earnshaw, P., Persson, P. O. G., Milton, S. F., and Leck, C.: Modelling atmospheric structure, cloud and their response to CCN in the central Arctic: ASCOS case studies, *Atmos. Chem. Phys.*, 12, 3419–3435, doi:10.5194/acp-12-3419-2012, 2012.
- Chapman, W. L. and Walsh, J. E.: Simulations of Arctic temperature and pressure by global coupled models, *J. Climate*, 20, 609–632, doi:10.1175/JCLI4026.1, 2007.
- Curry, J. A. and Ebert, E. E.: Annual cycle of radiative fluxes over the Arctic Ocean: Sensitivity to cloud optical properties, *J. Climate*, 5, 1267–1280, 1992.
- Devasthale, A., Sedlar, J., and Tjernström, M.: Characteristics of water-vapour inversions observed over the Arctic by Atmospheric Infrared Sounder (AIRS) and radiosondes, *Atmos. Chem. Phys.*, 11, 9813–9823, doi:10.5194/acp-11-9813-2011, 2011.
- Gascard, J.-C., Festy, J., le Goff, H., Weber, M., Brummer, B., Offermann, M., Doble, M., Wadhams, P., Forsberg, R., Hanson, S., Skourup, H., Gerland, S., Nicolaus, M., Metaxian, J.-P., Grangeon, J., Haapala, J., Rinne, E., Haas, C., Heygster, G., Jakobson, E., Palo, T., Wilkinson, J., Kaleschke, L., Claffey, K., Elder, B., and Bottenheim, J.: Exploring Arctic transpolar drift during dramatic sea ice retreat, *Eos, Trans. Amer. Geophys. Union*, 89, 21–22, 2008.
- Holland, M. M. and Bitz, C. M.: Polar amplification of climate change in coupled models, *Clim. Dynam.*, 21, 221–232, 2003.
- Holton, J.: *An Introduction to Dynamic Meteorology*, Academic Press, 1992.
- Intrieri, J. M., Shupe, M. D., Uttal, T., and McCarty, B. J.: An annual cycle of Arctic clouds characteristics observed by radar and lidar at SHEBA, *J. Geophys. Res.*, 107, 8039, doi:10.1029/2000JC000423, 2002a.
- Intrieri, J. M., Fairall, C. W., Shupe, M. D., Persson, P. O. G., Andreas, E. L., Guest, P. S., and Moritz, R. E.: An annual cycle of Arctic surface cloud forcing at SHEBA, *J. Geophys. Res.*, 107, 8039, doi:10.1029/2000JC000439, 2002b.
- IPCC: *Climate Change 2007: The Physical Science Basis*, Contribution of Working Group I to the Fourth Assessment Report of the Intergovernmental Panel on Climate Change, edited by: Solomon, S., Qin, D., Manning, M., Chen, Z., Marquis, M., Averyt, K. B., Tignor, M., and Miller, H. L., Cambridge University Press, Cambridge, United Kingdom and New York, NY, USA, 2007.
- Kahl, J. D., Martinez, D. A., and Zaitseva, N. A.: Long-term variability in the low level inversion layer over the Arctic Ocean, *Int. J. Climate*, 16, 1297–1313, 1996.
- Kahl, J. D., Zaitseva, N. A., Khattatov, V., Schnell, R. C., Bacon, D. M., Bacon, J., Radionov, V., and Serreze, M. C.: Radiosonde observations from the former Soviet “North Pole” series of drifting ice stations, 1954–1990, *B. Am. Meteorol. Soc.*, 80, 2019–2026, doi:10.1175/1520-0477(1999)080<2019:ROFTFS>2.0.CO;2, 1999.

- Karlsson, J. and Svensson, G.: The simulation of Arctic clouds and their influence on the winter surface temperature in present-day climate in the CMIP3 multi-model dataset, *Clim. Dynam.*, 36, 623–635, doi:10.1007/s00382-010-0758-6, 2010.
- Kay, J. E. and Gettelman, A.: Cloud influence on and response to seasonal Arctic sea ice loss, *J. Geophys. Res.*, 114, D18204, doi:10.1029/2009JD011773, 2009.
- Kay, J. E., L'Ecuyer, T., Gettelman, A., Stephens, G., and O'Dell, C.: The contribution of cloud and radiation anomalies to the 2007 Arctic sea ice extent minimum, *Geophys. Res. Lett.*, 35, L08503, doi:10.1029/2008GL033451, 2008.
- Leck, C., Bigg, E. K., Covert, D. S., Heintzenberg, J., Maenhaut, W., Nilsson, E. D., and Wiedensohler, A.: Overview of the atmospheric research program during the International Ocean Expedition of 1991 (IAOE-1991) and its scientific results, *Tellus B*, 48, 136–155, 1996.
- Leck, C., Nilsson, E. D., Bigg, E. K., and Bäcklin, L.: The atmospheric program of the Arctic Ocean Expedition 1996 (AOE-1996) – an overview of scientific objectives, experimental approaches and instruments, *J. Geophys. Res.*, 106, 32051–32067, 2001.
- Leck, C., Tjernström, M., Matrai, P., and Swietlicki, E.: Microbes, clouds and climate: Can marine microorganisms influence the melting of the Arctic pack ice?, *EOS, Trans. Amer. Geophys. Union*, 85, 25–36, 2004.
- Lindsay, R. W. and Zhang, J.: The thinning of Arctic sea ice 1988–2003: Have we passed a tipping point?, *J. Climate*, 18, 4879–4894, 2005.
- Liu, Y., Key, J. R., and Wang, X.: The influence of changes in cloud cover on recent surface temperature trends in the Arctic, *J. Climate*, 21, 705–715, 2008.
- Moran, K. P., Martner, B. E., Post, M. J., Kropfli, R. A., Welsh, D. C., and Widener, K. B.: An unattended cloud-profiling radar for use in climate research, *B. Am. Meteorol. Soc.*, 79, 443–455, 1998.
- Overland, J. E.: The case for global warming in the Arctic, in: Influence of climate change on the changing Arctic and Sub-Arctic conditions, edited by: Nihoul, J. C. J. and Kostianoy, A. G., Nato Science for Peace and Security Series – C: Environmental Security, Springer, The Netherlands, 2009.
- Overland, J. E., Wang, M., and Salo, S.: The recent Arctic warm period, *Tellus*, 60, 589–597, doi:10.1111/j.1600-0870.2008.00327.x, 2008.
- Persson, P. O. G., Fairall, C. W., Andreas, E. L., Guest, P. S., and Perovich, D. K.: Measurements near the Atmospheric Surface Flux Group tower at SHEBA: Near-surface conditions and surface energy budget, *J. Geophys. Res.*, 107, 8045, doi:10.1029/2000JC000705, 2002.
- Richter-Menge, J. and Jeffries, M.: The Arctic, in “State of the Climate in 2010”, *B. Am. Meteorol. Soc.*, 92, S143–S160, 2011.
- Rigor, I. G., Colony, R. L., and Martin, S.: Variations in surface air temperature observations in the Arctic 1979–1997, *J. Climate*, 13, 896–914, 2000.
- Sedlar, J. and Tjernström, M.: Stratiform Cloud – Inversion Characterization During the Arctic Melt Season, *Bound.-Lay. Meteorol.*, 132, 455–474, doi:10.1007/s10546-009-9407-1, 2009.
- Sedlar, J., Tjernström, M., Mauritsen, T., Shupe, M. D., Brooks, I. M., Persson, P. O. G., Birch, C. E., Leck, C., Sirevaag, A., and Nicolaus, M.: A transitioning Arctic surface energy budget: the impacts of solar zenith angle, surface albedo and cloud radiative forcing, *Clim. Dynam.*, 37, 1643–1660, doi:10.1007/s00382-010-0937-5, 2011.
- Sedlar, J., Shupe, M. D., and Tjernström, M.: On the relationship between thermodynamic structure and cloud top, and its climate significance in the Arctic, *J. Climate*, 25, 2374–2393, doi:10.1007/s00382-010-0937-5, 2012.
- Serreze, M. C. and Francis, J.: The Arctic Amplification Debate, *Climatic Change*, 76, 241–264, 2006.
- Serreze, M. C., Kahl, J. D., and Schnell, R. C.: Low-level temperature inversions of the Eurasian Arctic and comparisons with Soviet drifting station data, *J. Climate*, 5, 615–629, 1992.
- Serreze, M. C., Holland, M. M., and Stroeve, J.: Perspectives on the Arctic's shrinking sea-ice cover, *Science*, 315, 1533–1536, doi:10.1126/science.1139426, 2007.
- Shupe, M. D. and Intrieri, J. M.: Cloud radiative forcing of the Arctic surface: The influence of cloud properties, surface albedo, and solar zenith angle, *J. Climate*, 17, 616–628, 2004.
- Shupe, M. D., Uttal, T., and Matrosov, S. Y.: Arctic cloud microphysics retrievals from surface-based remote sensors at SHEBA, *J. Appl. Meteorol.*, 44, 1544–1562, 2005.
- Shupe, M. D., Walden, V. P., Eloranta, E., Uttal, T., Campbell, J. R., Starkweather, S. M., and Shiobara, M.: Clouds at Arctic Atmospheric Observatories, Part I: Occurrence and macrophysical properties, *J. Appl. Meteorol. Clim.*, 50, 626–644, 2011.
- Sirevaag, A., de la Rosa, S., Fer, I., Nicolaus, M., Tjernström, M., and McPhee, M. G.: Mixing, heat fluxes and heat content evolution of the Arctic Ocean mixed layer, *Ocean Sci.*, 7, 335–349, doi:10.5194/os-7-335-2011, 2011.
- Solomon, A., Shupe, M. D., Persson, P. O. G., and Morrison, H.: Moisture and dynamical interactions maintaining decoupled Arctic mixed-phase stratocumulus in the presence of a humidity inversion, *Atmos. Chem. Phys.*, 11, 10127–10148, doi:10.5194/acp-11-10127-2011, 2011.
- Sorteberg, A., Furevik, T., Drange, H., and Kvamstø, N. G.: Effects of simulated natural variability on Arctic temperature projections, *Geophys. Res. Lett.*, 32, L18708, doi:10.1029/2005GL023404, 2005.
- Tjernström, M.: The summer Arctic boundary layer during the Arctic Ocean Experiment 2001 (AOE-2001), *Bound.-Lay. Meteorol.*, 117, 5–36, 2005.
- Tjernström, M.: Is there a diurnal cycle in the summer cloud-capped Arctic boundary layer?, *J. Atmos. Sci.*, 64, 3970–3986, 2007.
- Tjernström, M. and Graversen, R. G.: The vertical structure of the lower Arctic troposphere analysed from observations and ERA-40 reanalysis, *Q. J. Roy. Meteor. Soc.*, 135, 431–433, 2009.
- Tjernström, M., Leck, C., Persson, P. O. G., Jensen, M. L., Oncley, S. P., and Targino, A.: The summertime Arctic atmosphere: Meteorological measurements during the Arctic Ocean Experiment (AOE-2001), *B. Am. Meteorol. Soc.*, 85, 1305–1321, 2004a.
- Tjernström, M., Leck, C., Persson, P. O. G., Jensen, M. L., Oncley, S. P., and Targino, A.: Experimental equipment: An electronic supplement to “The summertime Arctic atmosphere: Meteorological measurements during the Arctic Ocean Experiment (AOE-2001)”, *B. Am. Meteorol. Soc.*, 85, 1322–1322, 2004b.
- Tjernström, M., Zagar, M., Svensson, G., Cassano, J. C., Pfeifer, S., Rinke, A., Wyser, K., Dethloff, K., Jones, C., Semmler, T., and Shaw, M.: Modelling the Arctic boundary layer: An evaluation of six ARCMIP regional-scale models using data from the SHEBA

- project, Bound.-Lay. Meteorol., 117, 337–381, 2005.
- Tjernström, M., Sedlar, J., and Shupe, M. D.: How well do regional climate models reproduce radiation and clouds in the Arctic?, *J. Appl. Meteorol. Clim.*, 47, 2405–2422, 2008.
- Uttal, T., Curry, J. A., McPhee, M. G., Perovich, D. K., Moritz, R. E., Maslanik, J. A., Guest, P. S., Stern, H. L., Moore, J. A., Turenne, R., Heiberg, A., Serreze, M. C., Wylie, D. P., Persson, P. O. G., Paulson, C. A., Halle, C., Morison, J. H., Wheeler, P. A., Makshtas, A., Welch, H., Shupe, M. D., Intrieri, J. M., Stamnes, K., Lindsey, R. W., Pinkel, R., Pegau, W. S., Stanton, T. P., and Grenfeld, T. C.: Surface Heat Budget of the Arctic Ocean, *B. Am. Meteorol. Soc.*, 83, 255–276, 2002.
- Vihma, T., Jaagus, J., Jakobson, E., and Palo, T.: Meteorological conditions in the Arctic Ocean in spring and summer 2007 as recorded on the drifting ice station Tara, *Geophys. Res. Lett.*, 35, L18706, doi:10.1029/2008GL034681, 2008.
- Walsh, J., Kattsov, V., Chapman, W., Govorkova, V., and Pavlova, T.: Comparison of Arctic climate simulations by uncoupled and coupled global models, *J. Climate*, 15, 1429–1446, 2002.
- Wang, X. and Key, J. R.: Arctic Surface, Cloud, and Radiation Properties Based on the AVHRR Polar Pathfinder Data Set, Part I: Spatial and Temporal Characteristics, *J. Climate*, 18, 2558–2574, 2005.
- Westwater, E. R., Han, Y., Irisov, V. G., Leuskiy, V., Kadyrov, E. N., and Viazankin, S. A.: Remote sensing of boundary layer temperature profiles by a scanning 5-mm microwave radiometer and RASS: Comparison experiments, *J. Atmos. Ocean. Tech.*, 16, 805–818, 1999.
- Westwater, E. R., Han, Y., Shupe, M. D., and Matrosov, S. Y.: Analysis of integrated cloud liquid and precipitable water vapor retrievals from microwave radiometers during SHEBA, *J. Geophys. Res.*, 106, 32019–32030, 2001.
- White, A. B., Jordan, J., Martner, B., Ralph, F., and Bartram, B.: Extending the dynamic range of an S-band radar for cloud and precipitation studies, *J. Atmos. Ocean. Tech.*, 17, 1226–1234, 2000.